

THESIS FOR THE DEGREE OF LICENTIATE OF ENGINEERING

Effective Field Theory and One-proton Halo Nuclei

EMIL RYBERG



Department of Fundamental Physics
CHALMERS UNIVERSITY OF TECHNOLOGY
Göteborg, Sweden 2014

Effective Field Theory and One-proton Halo Nuclei
EMIL RYBERG

© EMIL RYBERG, 2014

Department of Fundamental Physics
Chalmers University of Technology
SE-412 96 Göteborg
Sweden
Telephone +46 (0)31-772 1000

Cover:

A leading-order Feynman diagram from the effective field theory description of radiative capture reactions. The direction of time is from right to left. See Chapters 3.1.4 and 3.2.4 for details.

Chalmers Reproservice
Göteborg, Sweden 2014

Effective Field Theory and One-proton Halo Nuclei
EMIL RYBERG
Department of Fundamental Physics
Chalmers University of Technology

Abstract

In this thesis we present formalism for treating one-proton halo nuclei in effective field theory. Halo nuclei are loosely bound systems consisting of a core plus valence nucleon(s). In so called Halo, or Cluster, effective field theory, the core of the halo nucleus is treated as a structureless, effective degree-of-freedom. As such, Cluster effective field theory is a low-energy model, appropriate for typical momentum scales of halo physics. The advantages of using effective field theory are the systematic way of improving results, by including higher orders, and the rigorous error estimates at each order. The observables that we consider are the charge form factor and the radiative capture cross section. A leading-order correlation between these observables is also derived. The framework is presented to next-to-leading order for S-wave interactions and to leading order for P-wave interactions.

The formalism is exemplified by applying it to study the one-proton halo states $^{17}\text{F}^*$ and ^8B . Results are presented for the charge radii of these systems and the S-factors of the radiative capture reactions $^{16}\text{O}(p, \gamma)^{17}\text{F}^*$ and $^7\text{Be}(p, \gamma)^8\text{B}$. The S-factor results compare well with data and previous calculations.

Keywords: effective field theory, nuclear physics, halo nuclei, radiative capture, charge radius

This thesis is based on work from the following three papers. In the main text these papers will be referred to as Paper 1, Paper 2 and Paper 3, respectively.

Paper 1:

Effective field theory for proton halo nuclei

Emil Ryberg, Christian Forssén, Hans-Werner Hammer and Lucas Platter

Phys. Rev. C89 (2014) 014325, e-Print: arXiv:1308.5975

In this paper we introduce formalism in Halo effective field theory for treating one-proton halo nuclei bound due to an S-wave interaction. The formalism is applied to study the excited state of ^{17}F and results are presented for the charge radius of $^{17}\text{F}^*$ and the S-factor for the radiative capture reaction $^{16}\text{O}(p, \gamma)^{17}\text{F}^*$.

Paper 2:

Constraining Low-Energy Proton Capture on Beryllium-7 through Charge Radius Measurements

Emil Ryberg, Christian Forssén, Hans-Werner Hammer and Lucas Platter

Submitted to Eur. Phys. Jour. A, e-Print: arXiv:1406.6908

Here, we extend the effective field theory formalism to treat charged systems bound due to a P-wave interaction. In this paper the one-proton halo ^8B is considered. The main result of this paper is the correlation between the charge radius of ^8B and the threshold S-factor of the radiative capture reaction $^7\text{Be}(p, \gamma)^8\text{B}$.

Paper 3:

Range corrections in proton halo nuclei

Emil Ryberg, Christian Forssén, Hans-Werner Hammer and Lucas Platter

Manuscript in preparation

This paper is a continuation of Paper 1. We go into more detail on the Halo effective field theory formalism for systems bound in the presence of a strong Coulomb repulsion. Also, the calculations are extended to include next-to-leading order effects, in the form of effective-range corrections.

Contents

1	Introduction	1
1.1	Halo physics	4
1.2	Effective field theory	5
2	Halo/Cluster effective field theory	11
2.1	One-neutron halos in effective field theory	13
2.1.1	Interactions and Feynman rules	14
2.1.2	Renormalization and matching to the effective range expansion	15
3	One-proton halos in effective field theory	19
3.1	S-wave one-proton halo nuclei – The $^{17}\text{F}^*$ state	20
3.1.1	Interactions	20
3.1.2	Fixing parameters	25
3.1.3	The charge form factor	26
3.1.4	Radiative capture and the astrophysical S-factor	31
3.2	P-wave one-proton halo nuclei – The ^8B nucleus	35
3.2.1	Interactions	35
3.2.2	Fixing parameters	38
3.2.3	The charge form factor	41
3.2.4	Radiative capture	43
3.2.5	Correlating the threshold S-factor and charge radius of ^8B	48
4	Discussion and outlook	51
A	Coulomb effects in effective field theory	53
A.1	Partial-wave projected Coulomb Green’s function	55

B	Proton halo diagrams	59
B.1	Elastic scattering and bound state properties for an S-wave interaction	59
B.2	Radiative capture diagrams for an S-wave interaction	61
B.3	P-wave interactions	62
B.3.1	Elastic scattering and bound state properties	65
B.4	P-wave charge form factor	68
B.4.1	Charge form factor diagrams	68
B.4.2	Normalization of the charge radius	70
B.4.3	The charge radius	71

Chapter 1

Introduction

This licentiate thesis presents an application of effective field theory to the exotic nuclear systems known as halo nuclei, or more precisely to one-proton halo nuclei. In this first chapter we will introduce concepts of nuclear physics and effective field theory (EFT) that will be relevant for the remainder of the thesis.

Nuclear physics is the field in which the constituents of atomic nuclei and their interactions are studied. The basic constituents of nuclei are nucleons, but through the interactions of nucleons, mediated by for example pions, one might argue that the ingredients of an atomic nucleus are more involved. One can think of the nucleus as consisting of nucleons living in a sea of pions. As such, the notions of constituents and interactions are tied tightly together. We will therefore introduce the concept of degree-of-freedom, which is very similar to that of constituent, with the difference that a degree-of-freedom is something that is chosen; it is one of the ingredients that define the model we are working with to describe Nature. Thus, with a given number of degrees-of-freedom one can write down all the possible interactions between these. For example, a model with only the nucleons as degrees-of-freedom will only have contact interactions between these nucleons, while a model with pions included will also have pion-nucleon and pion-pion interactions.

In Nature we have a large amount of different mesons, and there are also excitations of the nucleons that could be included as degrees-of-freedom. This raises questions about how the degrees-of-freedom should be chosen; should quarks and gluons be included? The quarks are confined within the nucleon and are only made visible on the GeV scale, a scale high enough for nucleons to be created out of vacuum. Therefore, quarks and gluons are not directly relevant degrees-of-freedom for nuclear physics. Though, for example in Chiral effective field theory, the symmetries of QCD are used to constrain the possible interactions between nucleons and mesons. Note also that even

though quarks and gluons are not relevant degrees-of-freedom for nuclear physics, it is a necessity to understand how these combine into nucleons and mesons, if one wants to bridge the gap between QCD and nuclear physics.

What about a model with only nucleons as degrees-of-freedom? Such a model would, as stated above, only have contact interactions between the nucleons. These contact interactions have a typical range of ~ 1 fm, since the nucleons are extended objects with this size. In such a model, with only nucleons as degrees-of-freedom, we can not really ask questions about the internal structure of the nucleons, since then we will run into pion-physics as the pion mass is about $140 \text{ MeV} = (1.4 \text{ fm})^{-1}$ ¹. In a sense, the nucleon-only model breaks down around the momentum scale 140 MeV or the length scale 1.4 fm. Can such a nucleon-only model still be useful for nuclear physics?

In nuclear physics a typical momentum scale is around the pion mass which can be seen from the fact that the typical binding energy per nucleon is around or below $B \sim 10$ MeV, translating into a momentum scale $\sqrt{mB} \sim 100$ MeV, where $m \approx 939$ MeV is the nucleon mass. There are a few systems though, that can be said to have a significantly lower momentum scale. The obvious example is the deuteron, which consists of a neutron and a proton bound together by only 2.2 MeV. Thus, for the deuteron the relevant momentum scale is of the order 45 MeV. However, for a system such as ${}^4\text{He}$, where the one-nucleon separation energies and the excited states are around 20 MeV, the relevant momentum scale is around 140 MeV. This means that ${}^2\text{H}$ can be described using only nucleons, since the relevant momentum scale is smaller than the pion mass, while ${}^4\text{He}$ can not. In this sense it becomes apparent that together with the choice of degrees-of-freedom is also an implicit choice of breakdown scale for the model. The concept of breakdown scale is of key importance for effective theories, which we will discuss below.

A defining property of nuclear physics is also what the relevant observables are, that is the quantities that theorists calculate and experimentalists measure. The most basic observable of nuclear physics is energies: binding energies, excitation energies, and so on, for example the 2.2 MeV binding energy of the deuteron and the first excited state energy of ${}^7\text{Be}$ at 0.43 MeV. Discrete quantum numbers, such as nuclear spin J and parity $\pi = \pm$, are of course also very relevant and these are usually combined in the notation J^π . Further, size and shape observables, such as the charge radius and deformation, are standard. The observables listed above are examples of nuclear structure observables, also called static observables. There are also dynamic observables, that is observables having to do with nuclear reactions. These

¹We work in units where $\hbar = c = 1$ and we use $\text{MeV fm} = 197.327$ to convert energy into length.

can for example be transfer reactions, capture reactions and elastic scattering. In this thesis we will present results for charge radii, elastic scattering and radiative capture cross sections, while we use energy levels and nucleon separation energies, together with J^π quantum numbers, as input for the calculations.

As have already been introduced above, the concept of basic constituents of the nucleus, or choice of degrees-of-freedom for the problem at hand, will in a sense define what possible interactions should be present in the chosen model and will also set some limits on the possible accuracy that can be achieved. It is at this stage of the thesis that we introduce effective theories, as a tool to understand nuclear physics, or physics in general. Effective theories take the view that questions about a physical property come also with a statement of the scale at which the property is measured, or viewed. For example, if asking about the potential energy due to the pull of the Earth one should also state at what height above the Earth surface (at radius R), the question is asked. This, since for high altitudes h above the ground one must use Newton's law of gravitation $V = -GM/(R+h) + GM/R$, while close to the surface of the Earth the effective theory using the standard gravity g gives the simpler answer $V_{\text{eff}} = hg$. Of course, expanding Newton's law of gravitation for $h \ll R$, we reproduce the effective standard gravity potential, with $g = GM/R^2$, together with higher-order corrections in powers of h/R . For a large scale separation $h \ll R$ the effective description is therefore very accurate and the result can be systematically improved by including higher-order corrections. However, around $h \sim R$ all the terms in the h/R expansion will be of comparable size and therefore we say that the effective picture breaks down at the length scale R . These key concepts: effective description, separation of scales, higher-order corrections, systematic improvement and breakdown scale, are central for the method and results of this thesis. This discussion of effective theories as a way to view physics sets the foundation for the introduction of EFT below in Section 1.2.

The thesis is organized as follows: In the remainder of this introductory section we discuss halo physics and EFT. In Chapter 2 we describe Halo, or Cluster, EFT and exemplify by showing a derivation of the renormalization of the theory and the matching to low-energy elastic scattering parameters. Chapter 3 is the main part of this thesis, where our work on one-proton halo nuclei, using Halo EFT, is presented. The observables that we consider are charge radii, radiative capture cross sections and low-energy elastic scattering parameters. The first part of Chapter 3, on S-wave one-proton halo nuclei, is based on Paper 1 and Paper 3, and the second part, on P-wave one-proton halo nuclei, is based on Paper 2. In Chapter 4 we summarize the thesis with a discussion of Halo EFT and our results, and provide an outlook. Formulas

for Coulomb effects in EFT are presented in Appendix A and the evaluation of the diagrams relevant for the presented proton halo observables are given in Appendix B.

1.1 Halo physics

The word halo comes from the ancient Greek word hálōs , which is used to describe the optical phenomenon of a circle of light around the sun or the moon. In nuclear physics a halo nucleus denotes a nucleus that has a few of the nucleons in the nucleus located at larger distances than the remaining core nucleons. One says that these outer nucleons form a nuclear halo around the core. Halo states were first discovered by Tanihata et al [1] and Hansen and Jonson [2]. In Nature there are both one-nucleon and many-nucleon halos, for example the one-neutron halo nucleus ^{11}Be , which can be seen as consisting of a tightly bound ^{10}Be core and a loosely bound single neutron, and the two-neutron halo ^6He , consisting of two valence neutrons orbiting the ^4He core. For an early review on halo physics, see for example Ref. [3].

However, the statement that a few of the nucleons are located in a halo around the core has not been completely accurate. We can not really measure the position of individual nucleons in the nucleus. What we mean is strictly speaking that the wavefunction of the halo nucleus is very extended compared to the wavefunction of the core by itself, and that the outer nucleons are very loosely bound. Connecting this situation to observables one can, for example, characterize a halo nucleus by properties such as a large charge radius and small one-nucleon, or few-nucleon, separation energies.

A typical one-nucleon halo nucleus consists of a tightly bound core with a loosely bound nucleon attached; typically the one-nucleon separation energy is around $S_N \sim 0.1\text{--}1$ MeV. The core itself consists of several nucleons and these inner nucleons have momenta which are nuclear-physics-like, that is of order the pion mass. The point here is that the momentum of the valence nucleon, with respect to the core, is very small. Thus, viewing the core as structureless, the relevant momentum scale for the nuclear halo is $\sqrt{mS_N} \sim 10\text{--}30$ MeV, which is much smaller than the pion mass. The question then is whether it is actually permissible to treat the core as structureless or, at least, to which level of accuracy such a treatment works.

1.2 Effective field theory

EFT, as the name suggests, gives an effective description of Nature in terms of effective degrees-of-freedom. With effective we mean that we do not necessarily include all fundamental particles explicitly in our model, but modify interaction potentials to account for those missing particles. For example, weak-decay processes can be considered without using explicit vector bosons as force-mediating particles, as was done by Fermi and others in the 1930s. This was done using an effective coupling strength, the Fermi coupling G_F , which can be given in terms of the coupling constant of the weak force and the mass of the vector boson. That is, even though the vector bosons are not explicitly included, the interaction strengths does depend on the underlying physics. Other examples, from nuclear physics, would be the Pionless EFT, where the only explicit degrees-of-freedom are nucleons, and the Chiral EFT, where also pions are included. We will discuss the Pionless EFT in more detail below.

The first thing to note about EFTs is that they only describe the physics below a certain high-momentum scale, which we will denote k_{hi} . The momentum k_{hi} is called the breakdown scale of the EFT. Having defined the breakdown scale, one should then include all possible degrees-of-freedom below k_{hi} and exclude all the high-momentum degrees-of-freedom. The excluded degrees-of-freedom, usually referred to as short-range physics, are implicitly included in the EFT in the form of low-energy constants and short-range operators. The high-energy physics can be said to have been integrated out and this leaves a mark on the remaining long-range model through the modification of the interactions. To be able to remove the high-momentum physics and to define an EFT, there must be a separation of scales $k_{\text{lo}} \ll k_{\text{hi}}$, where k_{lo} is a low-momentum scale associated with the physics described by the EFT. The reason why such a separation of scales is necessary is a matter of resolution, which can be visualized by thinking in terms of wave lengths: If we measure a small object with low-momentum light, we will not be able to resolve the internal structure of the object since the wave length is too large. For very low-momentum probes we might even not see the object as anything else than a point-like particle. Therefore, we are not able to resolve the short-range physics if the momentum is smaller than k_{hi} .

Above, we discussed the concept of effective theories shortly. However, in this thesis we use EFT, which means that we work in a quantum field theory, with Lagrangians and quantum fields. The quantum field theory formalism is frequently used for relativistic theories, for example the Standard Model for particle physics. However, in this thesis we will only work in the non-relativistic limit of quantum field theory, which in principle is equivalent to a

standard Schrödinger-equation formalism. The reason why we still choose to use quantum field theory is because it provides a more straightforward way to improve on the theory by including higher-order corrections systematically. For example, the concept of short-range operators is much more natural in a quantum field theory and therefore this framework is convenient for doing effective theories.

The Lagrangian² is an energy functional, with dimensions energy/volume = (momentum)⁴. The Lagrangian contains both the kinetic-energy density terms of all the included fields, and all the possible interaction terms between these fields. If we, for example, choose the nucleons as our only degrees-of-freedom, we will only have nucleon-nucleon interactions. For such a model the Lagrangian is

$$\mathcal{L} = N^\dagger \left[i\partial_t + \frac{\nabla^2}{2m} + \dots \right] N - N^\dagger N^\dagger \hat{V}_2 NN - N^\dagger N^\dagger N^\dagger \hat{V}_3 NNN - \dots, \quad (1.1)$$

where N is the nucleon field and \hat{V}_2 is the two-body interaction potential, \hat{V}_3 is the three-body interaction potential, and so on. In the Lagrangian (1.1) we have suppressed both spin and isospin indices on the nucleon fields as well as on the interaction potentials. The first term, in square brackets, is the kinetic term and the dots refer to relativistic corrections to the Schrödinger kinetic-energy operator. The dots at the far right indicate that there exist many-body interactions to arbitrary number of nucleons. Note, however, that only the \hat{V}_2 interaction potential will contribute if only two nucleons in total are present in the system.

Since the Lagrangian (1.1) has momentum dimension equal to four³, the nucleon field must have momentum dimension $3/2$. This in turn implies that the interaction potentials have negative momentum dimension, for example $[\hat{V}_2] = -2$. As such, the Lagrangian (1.1) describes a *non-renormalizable* field theory, in contrast to *renormalizable* field theories which only have interaction potentials of non-negative dimension. We have put the two different types of field theories, the *renormalizable* and the *non-renormalizable*, in italic in order not to confuse the names with the concept of renormalization: *Renormalizable* field theories only need a finite number of counterterms to be renormalized, that is only a finite number of parameters are needed in the theory to be able to make predictions. A *non-renormalizable* field theory, on

²When we use the word Lagrangian we really mean Lagrangian density.

³The dimensional analysis presented in this section concerns unit dimensions, for example MeV. This is not to be confused with the concept of scaling dimension, where for example the operator $\partial_0 \sim E = p^2/(2m)$ has scaling dimension 2 as it scales with the low-momentum scale squared.

the other hand, needs infinitely many terms in the Lagrangian to be renormalized, which at first glance is a severe issue when it comes to predictive power. It is not practically possible to fit infinitely many parameters.

However, if the interaction potentials are expanded in powers of momentum, in a $k_{\text{lo}}/k_{\text{hi}}$ expansion, only a finite number of parameters are actually needed for renormalization at each order in this expansion. The field theory can be renormalized order by order. For the pionless Lagrangian (1.1) the zeroth-order term of the S-wave two-body interaction would just be a constant in momentum space, and the next non-zero term would be given by a momentum-squared operator. In coordinate space, these first two interactions would correspond to a Dirac delta interaction, $\delta(\mathbf{r})$, and a nabla-squared acting on a Dirac delta, $\nabla^2\delta(\mathbf{r})$. Note however, that the Pionless EFT in the strong coupling regime is actually renormalized without any additional counter terms. We will show this explicitly in Chapter 2.1.2.

Thus, by expanding the interaction potentials in powers of momentum and keeping only the leading term, we arrive at what we denote leading-order (LO) in the EFT. As we have excluded contributions one order up in powers of $k_{\text{lo}}/k_{\text{hi}}$ we expect that this approximation generates an error that is proportional to this ratio. The momentum ratio $k_{\text{lo}}/k_{\text{hi}}$ is generally called the EFT expansion parameter and it provides the expected EFT error. If we choose to include the first two terms in the expansion we are doing a next-to-leading order (NLO) calculation, with expected EFT error $(k_{\text{lo}}/k_{\text{hi}})^2$; include an additional order and we are at next-to-next-to-leading order (N²LO), and so on. This way of organizing the EFT is called power counting.

For some observables we may run into a road block at a certain order in the form of a short-range operator, entering with an undetermined parameter which we can not fit to data. This can either be due to practical reasons, such as the lack of appropriate data, or formal reasons, such as the short-range parameter appearing only for the observable under consideration. In such a scenario one can say that there is an upper limit on the accuracy that the EFT can achieve. We will discuss such cases in Chapters 3.1.3 and 3.2.3.

Parallel to the EFT expansion is the effective range expansion (ERE). The ERE is a way to describe low-energy elastic scattering of two particles in terms of only a few low-energy elastic scattering parameters. These parameters are the scattering length a , the effective range r , the shape parameter P , and so on. The range of the interaction needs to be finite for the ERE to be well defined and the size of the ERE parameters is typically related to the range. The defining equation for the low-energy elastic scattering parameters is the momentum expansion of $\cot(\delta)$, where δ is the phase shift:

$$k^{2l+1} \cot(\delta_l) = -\frac{1}{a_l} + \frac{1}{2}r_l k^2 + P_l k^4 + \dots \quad (1.2)$$

In Eq. (1.2) we have included the angular momentum quantum number l as a subscript on the parameters and the phase shift, to make the defining equation more general.

The phase shift can be related to the differential elastic scattering cross section according to

$$\frac{d\sigma}{d\Omega} = \left| \frac{1}{k} \sum_{l=0}^{\infty} (2l+1) \exp(i\delta_l) \sin(\delta_l) P_l(\cos\theta) \right|^2, \quad (1.3)$$

where $P_l(x)$ is the l th Legendre polynomial. Eq. (1.3) implies that if a momentum expansion is made, and only the zeroth-order term is kept, then the total cross section in the low-momentum limit is given by

$$\sigma_{\text{tot}} \rightarrow 4\pi a_0^2. \quad (1.4)$$

Comparing Eq. (1.4) with a classical picture, with a geometrical cross section for the particles, then the $l = 0$ scattering length looks much like the radius of the particle in the extreme low-momentum regime. This geometrical picture is of course not correct in the quantum world of nuclear physics and the scattering length can be very different from the actual radius of the particle.

Coming back to EFTs, it is common to express the parameters in the EFT Lagrangian in terms of the low-energy scattering parameters. It is preferable to use actual observable quantities, such as scattering lengths and effective ranges, rather than non-observable ones, such as coefficients of the interaction terms, when discussing and analyzing the physics of the EFT. In EFTs for nuclear physics, the effective range typically scales with the high-momentum scale k_{hi} , which is to say that it scales naturally. The scattering length often scales unnaturally with the low-momentum scale k_{lo} . One would then say that the low-momentum scale emerges due to a fine-tuning in the underlying short-range physics. For example, for nucleon-nucleon elastic scattering the S-wave effective range is of the order a few femtometers, while the scattering length is of the order a few tens of femtometers in some channels. This shows the existence of a clear separation of scales in the nucleon-nucleon system, and it is this separation of scales that is the basis for many of the EFTs for nuclear physics.

In this thesis we will be concerned with the so called Halo EFT, or Cluster EFT, which is similar to the Pionless EFT in the sense that pions are excluded. However, in Halo EFT the relevant momentum scales are even lower than what they typically are in the Pionless EFT, since extremely loosely bound systems are considered. Actually, in Halo EFT not only nucleons, but also tightly bound clusters of nucleons, are used as effective degrees-of-freedom, which then puts a much more severe constraint on the model

through a lower breakdown scale. This scale can be associated with the momentum scale of the inner structure of these clusters. A hint of the typical breakdown scale for Halo EFT can be given by the size of the cluster in question: If for example the cluster has a radius of about 3 fm, then this defines the breakdown scale in length and it is translated into a momentum breakdown scale of 60–70 MeV.

Chapter 2

Halo/Cluster effective field theory

Halo EFT gives an effective description of halo nuclei by treating the core of the halo nucleus as an effective degree of freedom. This means that within this description the core has no internal structure; it is a basic constituent. However, it is clear that the core does consist of nucleons and therefore Halo EFT will not give a valid description of the system for momenta high enough to resolve this internal structure. This is actually not a severe restriction since much of the physics relevant to the characteristics of halo nuclei occur at very low momenta. Expressed in another way, there is a separation of scales present in halo systems such that the physics related to the structure of the core can be well separated from the relevant low-energy physics.

Halo EFT was proposed in Ref. [4] in the context of describing the two-neutron halo ${}^6\text{He}$. In this paper, the resonant ${}^4\text{He}+\text{neutron}$ system was studied, with the purpose of using ${}^5\text{He}$ as a stepping stone to the more interesting ${}^6\text{He}$ halo nucleus. Since then, this approach to study ${}^6\text{He}$ has continued with efforts by several authors [5, 6, 7]. Descriptions of other two-neutron halos, using Halo EFT, can be found in Refs. [8, 9]. Halo EFT has also been applied to one-nucleon halos and few-cluster systems. In Ref. [10] the electromagnetic properties of the one-neutron halo ${}^{11}\text{Be}$ were studied. Since then even more one-neutron halo nuclei have been analyzed, see Refs. [11, 12, 13]. The cluster systems that have been considered are the resonant α - α scattering [14] and the reaction $d + t \rightarrow n + \alpha$ [15]. The reason for Halo EFT to be applicable to these non-halo systems is the existence of a separation of scales and therefore, if one was to liberally stretch the concept of halo systems, the unbound nuclei ${}^5\text{He}$ and ${}^8\text{Be}$ can be considered as halo-like. A more appropriate name for the EFT is then arguably Cluster EFT, since clusters of nucleons are treated as basic constituents, and this is the name we will

use in the remainder of this thesis. Much of the work done in Cluster EFT builds on the pioneering work by Ref. [16].

Our work mainly regards the treatment of one-proton halo nuclei in Cluster EFT, such as ${}^8\text{B}$ and the excited state of ${}^{17}\text{F}$, and we will describe this in Chapter 3. The obvious difference from the previous work on one-neutron halo systems is that all the degrees-of-freedom are charged, and therefore that Coulomb repulsion needs to be taken into account. In many areas of physics, the Coulomb interaction can be included perturbatively, noting that the fine-structure constant $\alpha \approx 1/137$ is very small. However, there are two possible complications to this perturbative approach in nuclear physics. The Coulomb interaction in momentum space, for two particles with charges Z_1 and Z_2 and relative momentum k , is given by $Z_1 Z_2 \alpha / k^2$. It is therefore evident that: (i) if the charges are too large or (ii) if the momentum is too small, then a perturbative approach will break down. We proceed by defining the Coulomb momentum $k_C := Z_1 Z_2 \alpha m_R$, which gives a momentum scale corresponding to the inverse Bohr radius of the system. For the cases we will study $k_C \sim 20\text{--}50$ MeV. The perturbativeness can be incorporated into the Sommerfeld parameter, or Coulomb strength parameter, $\eta := k_C / k$. If $\eta > 1$ we say that we are in the deep non-perturbative regime. All systems considered in this work will have $\eta \gtrsim 1$, that is we will need to include the Coulomb interaction to all orders.

In Ref. [17] proton-proton scattering was considered within the Pionless EFT, with the Coulomb interaction included to all orders. This formalism has for example been used to accurately describe the weak proton-proton fusion process, see the review [18] and references therein. Our work extends this formalism to treat bound two-body systems, with a strong Coulomb repulsion, such as one-proton halo nuclei. The inclusion of the Coulomb repulsion brings in the additional momentum scale k_C , which together with the binding momentum γ defines the low-energy properties of the one-proton halo. This should be compared with the one-neutron halo system, where only the binding momentum is present and therefore sets the scale. In this context one should also mention that, for some systems, the inclusion of the effective range is needed due to renormalization issues (for P-wave interactions) [4] or fine-tunings of the physical parameters.

Using Cluster EFT we calculate low-energy observables for the one-proton halo states ${}^{17}\text{F}^*$ and ${}^8\text{B}$. The observables that we have considered so far are the charge radius and the radiative capture cross section. The charge radius of ${}^8\text{B}$ is of particular interest, since it is planned to be measured via an atomic isotope-shift measurement. The radiative capture processes ${}^{16}\text{O}(p, \gamma){}^{17}\text{F}^*$ and ${}^7\text{Be}(p, \gamma){}^8\text{B}$ are of astrophysical interest as the cross sections are used as input for nucleosynthesis calculations, see the review [19]. The reaction

${}^7\text{Be}(p, \gamma){}^8\text{B}$ is particularly interesting, since it determines the production of high-energy solar neutrinos.

2.1 One-neutron halos in effective field theory

In Chapter 3 we will consider charged-particle systems in Cluster EFT, where both the strong nuclear force and the Coulomb interaction need to be treated non-perturbatively. Before turning to these more involved systems we will consider one-neutron halo systems and exemplify the approach with a derivation of the matching between the coefficients of the EFT Lagrangian and the effective-range parameters.

One-neutron halo systems such as ${}^{11}\text{Be}$ and ${}^{19}\text{C}$ can be studied in Cluster EFT [10, 12]. In ${}^{11}\text{Be}$ there are two weakly bound states, the $1/2^+$ ground state with neutron separation energy $B_0 = 0.50$ MeV and the $1/2^-$ excited state with $B_1 = 0.18$ MeV. These halo states can be modeled as a ${}^{10}\text{Be}(0^+)$ core field and a valence neutron field n being in a relative S-wave or P-wave, respectively. The neutron separation energies are used to define the binding momenta for the ground state $\gamma_0 = \sqrt{2m_{\text{R}}B_0} = 29$ MeV, and for the excited state $\gamma_1 = \sqrt{2m_{\text{R}}B_1} = 18$ MeV, where m_{R} is the reduced mass of the systems. For a core of mass M and a neutron of mass m , the reduced mass is given by $m_{\text{R}} = Mm/(M + m)$. We treat the binding momenta as our low-momentum scales, that is $\gamma_0 \sim k_{\text{lo}}$ or $\gamma_1 \sim k_{\text{lo}}$.

It is important to question the assumption of a structureless ${}^{10}\text{Be}$ core field, that is if its internal structure is well separated from the momentum scales of the halo states. We do this by considering the first core excitation, which is a 2^+ state. The excitation energy is $E_1 = 3.4$ MeV, which defines a momentum scale corresponding to short-range physics $k_{\text{hi}} \sim \sqrt{2m_{\text{R}}E_1} = 76$ MeV. Thus, we note that we have a rather good separation of scales, with EFT expansion parameters $\gamma_0/k_{\text{hi}} \sim 0.4$ and $\gamma_1/k_{\text{hi}} \sim 0.2$, and that this separation is particularly good for the excited state of ${}^{11}\text{Be}$.

One should also consider possible resonant states in the ${}^{11}\text{Be}$ system, since these can give short-range contributions to, for example, radiative capture cross sections. The first resonance is a $5/2^+$ state, 1.78 MeV above the ground state. Thus, for observables where this resonance can contribute, it should define the breakdown scale of the EFT. To include the resonance explicitly in a radiative capture calculation one would need to either include D-wave mixing or the 2^+ core excitation.

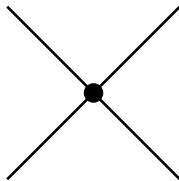


Figure 2.1: A schematic of the two-body interaction between the fields. The interaction strength is iC_0 .

2.1.1 Interactions and Feynman rules

In this section we derive the Feynman rules for a two-particle EFT for distinguishable particles, bound due to an unnaturally large S-wave scattering length. This type of model is applicable for the S-wave one-neutron halo system ^{11}Be , since the ^{10}Be core is a 0^+ state and the spin coupling is trivial.

The Lagrangian for two distinguishable particles, interacting only in the S-wave, is given by

$$\mathcal{L} = \psi_1^\dagger \left[i\partial_t + \frac{\nabla^2}{2m_1} \right] \psi_1 + \psi_2^\dagger \left[i\partial_t + \frac{\nabla^2}{2m_2} \right] \psi_2 + C_0 \psi_1^\dagger \psi_2^\dagger \psi_1 \psi_2 + \dots \quad (2.1)$$

The fields ψ_1 and ψ_2 have masses m_1 and m_2 , respectively, and the S-wave contact interaction has coefficient C_0 . The Lagrangian (2.1) is given at LO, with the dots referring to higher-order terms.

From the Lagrangian (2.1) we can extract the two propagators and the Feynman rule for the contact interaction. The propagators are given by the eigenvalues of the inverse kinetic energy operators, that is

$$iS_i(E, \mathbf{p}) = \frac{i}{E - \frac{\mathbf{p}^2}{2m_i} + i\varepsilon} \quad , \quad (2.2)$$

for $i = 1, 2$. The $+i\varepsilon$ piece in the propagators in Eq. (2.2) is needed to define the sense of time direction properly. In Fig. 2.1 the interaction between the fields is shown and the Feynman rule for this contact interaction is

$$iC_0 \quad . \quad (2.3)$$

Using the propagators (2.2) and the Feynman rule for the contact interaction (2.3) we are ready to calculate observables by evaluating the corresponding diagrams.

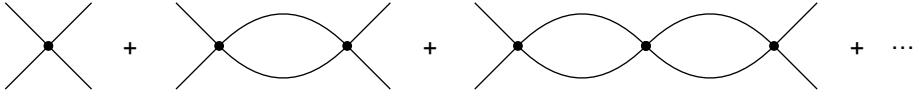


Figure 2.2: Elastic scattering diagrams, ordered in powers of the interaction strength iC_0 .

2.1.2 Renormalization and matching to the effective range expansion

As an example of the EFT for two distinguishable particles we derive the matching of the parameter C_0 to the unnaturally large scattering length. In doing this we will also show the renormalization needed at LO.

The elastic scattering t-matrix is typically expressed in terms of the phase shift, through the defining equation

$$T = -\frac{2\pi}{m_{\text{R}}} \frac{1}{k \cot(\delta) - ik} . \quad (2.4)$$

The S-wave phase shift is written as

$$k \cot(\delta) = -\frac{1}{a} + \frac{1}{2}rk^2 + \dots , \quad (2.5)$$

using the ERE given in Eq. (1.2). Combining Eqs. (2.4) and (2.5) we write the t-matrix using the effective-range parameters, according to

$$T = \frac{2\pi}{m_{\text{R}}} \frac{1}{\frac{1}{a} - \frac{1}{2}rk^2 + ik + \dots} . \quad (2.6)$$

In this section we will only be interested in the scattering length, which will be matched to the coefficient C_0 of the Lagrangian (2.1).

As we will see shortly, the theory must be strongly coupled for the scattering length to be unnaturally large. However, let us first assume that we are at weak coupling, such that we may consider the interaction C_0 perturbatively. The scattering t-matrix is then approximately given by only the first diagram in Fig. 2.2, with strength given completely by the Feynman rule (2.3). The t-matrix for this first-order perturbation is

$$iT^{(1)} = iC_0 , \quad (2.7)$$

that is a constant. Comparing Eqs. (2.6) and (2.7) it is evident that this first-order approximation is only valid at momenta that are very close to zero, but if the assumption that the interaction be weak is correct, we should be fine

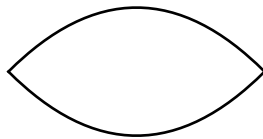


Figure 2.3: The irreducible self-energy loop-diagram.

at low momenta. Setting the momentum to zero and matching Eqs. (2.6) and (2.7) we find that

$$C_0 = \frac{2\pi a}{m_R} . \quad (2.8)$$

The result (2.8) is clearly contradictory, since we have assumed a weak coupling C_0 while having an unnaturally large scattering length a . This means that we are in fact in the strong coupling regime and need to proceed non-perturbatively.

Considering strong coupling we need to include all the diagrams of Fig. 2.2 at LO. This means that we have to evaluate diagrams involving loops, but for now we will just denote these loops by $i\Sigma(E)$ and proceed. Summing up all the diagrams, we have the full t-matrix

$$\begin{aligned} iT(E) &= iC_0 + iC_0 i\Sigma(E) iC_0 + iC_0 i\Sigma(E) iC_0 i\Sigma(E) iC_0 + \dots \\ &= \frac{iC_0}{1 + C_0 \Sigma(E)} , \end{aligned} \quad (2.9)$$

where we wrote the geometric series in closed form for convenience. The loop-diagram $\Sigma(E)$ is shown in Fig. 2.3 and it is called the irreducible self energy. It is given by an integral, summing up all the possible momentum flowing around the loop, as can be understood from the fact that momentum conservation at the vertices in the loop is not enough to constrain the momentum. In momentum space the irreducible self-energy is therefore given by an integral over the two propagators:

$$i\Sigma(E) = \int \frac{d^4 p}{(2\pi)^4} \frac{i}{E - p_0 - \frac{\mathbf{p}^2}{2m_1} + i\varepsilon} \frac{i}{p_0 - \frac{\mathbf{p}^2}{2m_2} + i\varepsilon} \quad (2.10)$$

Note that the energies $E - p_0$ and p_0 in the propagators could equivalently have been chosen as $E/2 - p_0$ and $E/2 + p_0$, since p_0 is just an integration variable that flows around the loop. We evaluate the p_0 -integral by a residue integration in the lower half-plane, around the pole at $p_0 = \mathbf{p}^2/(2m_2) - i\varepsilon$. Note that this integration gives a sign due to the orientation of the path. The result is

$$i\Sigma(E) = i \int \frac{d^3 p}{(2\pi)^3} \frac{1}{E - \frac{\mathbf{p}^2}{2m_R} + i\varepsilon} . \quad (2.11)$$

The integral (2.11) is formally divergent and we evaluate it using dimensional regularization in $3 - \epsilon$ dimensions (see for example Ref. [20]) in the power divergence subtraction (PDS) scheme [21], giving

$$i\Sigma(E) = -i\frac{m_{\text{R}}}{2\pi} \left[\sqrt{-E - i\epsilon} - \mu \right] , \quad (2.12)$$

where μ is the PDS regulator. For positive energy, $E = k^2/(2m_{\text{R}})$, the expression (2.12) is simplified to

$$i\Sigma(E) = i\frac{m_{\text{R}}}{2\pi} [ik + \mu] . \quad (2.13)$$

If we now use Eqs. (2.9) and (2.13) to match with Eq. (2.6) we find that the scattering length is given by

$$\frac{1}{a} = \frac{2\pi}{m_{\text{R}}C_0} + \mu . \quad (2.14)$$

Since the PDS regulator is present in Eq. (2.14), this is a renormalization condition, with the condition being that $\frac{2\pi}{m_{\text{R}}C_0} + \mu$ be finite; the divergence is absorbed by the parameter C_0 . Therefore, even though the interaction operator has negative momentum dimension, this field theory is renormalized without any need for counter terms. Note that in order to reproduce the effective range one needs to add an interaction $\sim C_2k^2$ in the Lagrangian.

Let us briefly return to the first-order result for weak coupling, Eq. (2.7). Including the second-order perturbation

$$\begin{aligned} i(T^{(1)} + T^{(2)}) &= iC_0 + iC_0i\Sigma(E)iC_0 \\ &= iC_0 \left(1 - C_0\frac{m_{\text{R}}}{2\pi} [ik + \mu] \right) \end{aligned} \quad (2.15)$$

and matching to Eq. (2.6) we run into a renormalization problem: The coefficient of ik in Eq. (2.15) must be finite and at the same time the regulator μ must be absorbed. This is not possible and it therefore calls for the appearance of a counterterm at this order. As such, the renormalization of *non-renormalizable* theories is made obvious. Note again, however, that for strong coupling the field theory was renormalized without any extra counter terms. This concludes the example on the renormalization of EFT for two distinguishable particles.

Chapter 3

One-proton halos in effective field theory

In the previous chapter, we introduced Cluster EFT and we demonstrated details on the renormalization of an S-wave interaction. For neutron halos, the only interaction is through the strong force, and due to a fine-tuning the system becomes very weakly bound. In this chapter we want to study one-proton halo nuclei using Cluster EFT and therefore we must also introduce the Coulomb interaction.

For some nuclear systems the Coulomb interaction can be treated as rather weak, compared to the strong interaction. However, for proton halo systems this is not possible since the relevant low-momentum scale k_{lo} of the system is of the same size or smaller than the Coulomb momentum $k_C = Z_c \alpha m_R$. What this means is that for proton halo nuclei the very small binding energy is a result of an interplay between the strong and the Coulomb interactions.

There are a few one-proton halo candidates in the chart of nuclides, for example the $1/2^+$ excited state of ^{17}F , which consists mostly of a proton and an $^{16}\text{O}(0^+)$ core in a relative S-wave. This excited state of ^{17}F has a proton separation energy of only 0.1 MeV, while the $5/2^+$ ground state is bound by 0.6 MeV. Since the first excitation of the ^{16}O core is at $E_1 = 6$ MeV, ^{17}F should be a perfect system to apply Cluster EFT on. Actually, both the ground state and the excited state are well separated from the momentum scale of the core excitation, and therefore both states can be treated in Cluster EFT. In this work we have only included the excited state $^{17}\text{F}^*$ into the field theory. We show results for the charge radius of $^{17}\text{F}^*$ and the radiative capture process $^{16}\text{O}(p, \gamma)^{17}\text{F}^*$ in Sec. 3.1. In order to also describe the ground state we would have to consider the D-wave nature of the interaction.

Other examples of proton halo nuclei in nature are the ^8B one-proton halo

nucleus, where a proton and a ${}^7\text{Be}$ core interact in a P-wave, and the two-proton halo ${}^{17}\text{Ne}$. To be able to treat two-proton halo nuclei one would need to derive three-body Coulomb propagators, which is beyond the present reach of our formalism. We have considered the P-wave one-proton halo nucleus ${}^8\text{B}$ and we have calculated the charge radius and the S-factor for the radiative capture cross section ${}^7\text{Be}(p, \gamma){}^8\text{B}$. These results are presented in Chapter 3.2. We also show a correlation between the charge radius and the S-factor. This system has also been considered recently in Ref. [22].

There has been some work on charged systems within EFT, starting with the efforts by Kong and Ravndal [23, 17, 24] and continuing with work on for example α - α scattering [14] in Cluster EFT and ${}^3\text{He}$ [25, 26] in Pionless EFT. Our work extends this list with one-proton halo nuclei, that is loosely bound two-body systems with a repulsive Coulomb interaction.

3.1 S-wave one-proton halo nuclei – The ${}^{17}\text{F}^*$ state

In this section we present Cluster EFT formalism for calculating the charge radius and the radiative capture cross section for a one-proton halo nucleus, bound by an S-wave interaction between the core and the proton fields. We exemplify this formalism by showing results for the one-proton halo state ${}^{17}\text{F}^*$. This section is based on the work presented in Papers 1 and 3.

3.1.1 Interactions

Using Cluster EFT we treat the one-proton halo state ${}^{17}\text{F}^*(1/2^+)$ as consisting of a proton and an ${}^{16}\text{O}(0^+)$ core in a relative S-wave. The proton and the ${}^{16}\text{O}$ core are therefore the effective degrees of freedom of the field theory.

Since the core is a 0^+ particle there is only one S-wave channel, namely $J = 1/2^+$, and thus the LO interaction is given by a single Dirac delta, $\delta(\mathbf{r})$. Higher-order interactions between the constituents come in as higher and higher powers of derivatives of the Dirac-delta, that is $\nabla^2\delta(\mathbf{r})$ and so on. By matching these interactions to low-energy scattering parameters of the S-wave Coulomb-modified ERE, see Eq. (B.3) in Appendix B.1,

$$kC_\eta^2(\cot \delta_0 - i) + 2k_C h_0(\eta) = -\frac{1}{a_0} + \frac{1}{2}r_0k^2 + Pk^4 + \dots, \quad (\text{B.3})$$

one finds that the Dirac delta interaction $\delta(\mathbf{r})$ gives the scattering length a_0 and the derivative interaction $\nabla^2\delta(\mathbf{r})$ enters with the effective range r_0 ,

as is derived in Appendix B.1. In Eq. (B.3) the Gamow-Sommerfeld factor $C_\eta^2 = 2\pi\eta/(\exp(2\pi\eta) - 1)$ and the function $h_0(\eta) = \psi(i\eta) + \frac{1}{2i\eta} - \log(i\eta)$ are introduced, where ψ is the polygamma function. Since each derivative scales as the low-momentum scale k_{lo} , the $\nabla^2\delta(\mathbf{r})$ interaction should be suppressed by two orders compared to the LO $\delta(\mathbf{r})$ interaction. However, for weakly bound systems such as halo nuclei, the scattering length is unnaturally large compared to the natural scaling k_{hi} . This implies that the $\nabla^2\delta(\mathbf{r})$ interaction is actually at NLO, as one can see from the Coulomb-modified ERE Eq. (B.3), using that $1/a_0 \sim k_{\text{lo}}$, $r_0 \sim 1/k_{\text{hi}}$ and $p \sim k_{\text{lo}}$. The next interaction term $\nabla^4\delta(\mathbf{r})$ enters at N³LO, assuming that the shape parameter scales naturally as $P \sim 1/k_{\text{hi}}^3$.

We will now treat the S-wave interaction using an auxiliary dicluster field in the Lagrangian. The Lagrangian for a spin-0 core and a proton, interacting only in the S-wave, using the dicluster field is given by

$$\begin{aligned} \mathcal{L} = & p_\sigma^\dagger \left(iD_t + \frac{\mathbf{D}^2}{2m} \right) p_\sigma + c^\dagger \left(iD_t + \frac{\mathbf{D}^2}{2M} \right) c + d_\sigma^\dagger \left[\Delta + \nu \left(iD_t + \frac{\mathbf{D}^2}{2M_{\text{tot}}} \right) \right] d_\sigma \\ & - g \left[d_\sigma^\dagger c p_\sigma + \text{h.c.} \right]. \end{aligned} \quad (3.1)$$

Here p_σ , with the spin index $\sigma = \pm 1/2$ denotes the spin-1/2 proton field with mass m and c the 0^+ core field with mass M . The covariant derivatives are defined as $D_\mu = \partial_\mu + ie\hat{Q}A_\mu$, with $\hat{Q}p_\sigma = p_\sigma$, $\hat{Q}c = Z_c c$ and $\hat{Q}d_\sigma = (Z_c + 1)d_\sigma$, where Z_c is the proton number of the core. The operator \hat{Q} is simply the charge operator. The dicluster field d_σ has mass M_{tot} and the vertex, where the dicluster field breaks up into a proton and a core, has strength g . The parameter Δ is called the residual mass of the dicluster and it is needed for renormalization of the S-wave interaction. The energy signature $\nu = \pm 1$ of the kinetic term of the dicluster field is present to allow for the possibility of a positive effective range, since we use the convention where the coupling g is real.

From the Lagrangian (3.1) we extract the Feynman rules for the propagators and the interactions. Firstly, the proton, core and the bare dicluster propagators are given by the inverse of the kinetic terms in Eq. (3.1). This gives the proton propagator

$$iS_p(E, \mathbf{p}) = \frac{i}{E - \frac{\mathbf{p}^2}{2m} + i\varepsilon}, \quad (3.2)$$

the core propagator

$$iS_c(E, \mathbf{p}) = \frac{i}{E - \frac{\mathbf{p}^2}{2M} + i\varepsilon} \quad (3.3)$$

and the bare dicluster propagator

$$iD^{(0)}(E, \mathbf{p}) = \frac{i}{\Delta + \nu \left(E - \frac{\mathbf{p}^2}{2M_{\text{tot}}} + i\varepsilon \right)}. \quad (3.4)$$

This dicluster propagator is called bare, since it will be dressed by proton-core loops and thereby gain an additional energy dependence in the denominator.

There is only one contact interaction vertex, which is given by the $d_{\sigma}^{\dagger} c p_{\sigma}$ term, and its coefficient is $-g$. The Feynman rule is given by

$$-ig. \quad (3.5)$$

In addition we have three vertices, where an A_0 photon interacts with the matter fields, which happens through the $iD_t = i\partial_t - e\hat{Q}A_0$, or νiD_t , operators. Thus we have the Feynman rules for the A_0 photon interaction with the proton

$$-ie, \quad (3.6)$$

the core

$$-ieZ_c \quad (3.7)$$

and the dicluster

$$-ive(Z_c + 1). \quad (3.8)$$

The dicluster-photon interaction can be thought of as a two-body current. Finally, we also have the vertices where a vector photon A_i couples to either of the matter fields. The responsible operators are $\frac{\mathbf{D}^2}{2m}$, $\frac{\mathbf{D}^2}{2M}$ and $\nu \frac{\mathbf{D}^2}{2M_{\text{tot}}}$, for interactions with the proton, core and dicluster, respectively. We chose to work in the Coulomb gauge, where $\nabla_i A_i = 0$, and therefore the \mathbf{D}^2 operator is expanded as $\mathbf{D}^2 = \nabla^2 + 2ie\hat{Q}A_i \nabla_i - e^2 \hat{Q}^2 A_i A_i$. In this work we will only consider vertices with one photon field and therefore, using $\nabla = i\mathbf{p}$, we arrive at the Feynman rules for the A_i photon interaction with the proton

$$-i \frac{ep_{\mathbf{p}}^i}{m}, \quad (3.9)$$

the core

$$-i \frac{eZ_c p_c^i}{M}, \quad (3.10)$$

and the dicluster

$$-i \frac{e(Z_c + 1)p_{\text{di}}^i}{M_{\text{tot}}}. \quad (3.11)$$

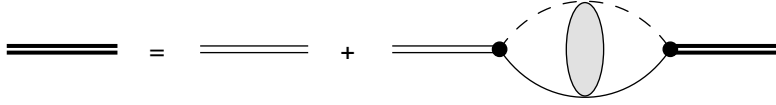


Figure 3.1: The full one-proton halo propagator, defined recursively using the bare halo propagator and the irreducible self-energy.

The momenta \mathbf{p}_p , \mathbf{p}_c and \mathbf{p}_{di} are the momenta of the proton, core and di-cluster, respectively. Defining the relative momentum

$$\mathbf{p} = \frac{M\mathbf{p}_p - m\mathbf{p}_c}{M_{\text{tot}}} \quad (3.12)$$

and positioning us in the center-of-mass (c.m.) frame, where $\mathbf{p}_p = -\mathbf{p}_c$, we have $\mathbf{p}_p = \mathbf{p} = -\mathbf{p}_c$. Note that for a single di-cluster field in the c.m. frame we have $\mathbf{p}_{di} = 0$, which means that the Feynman rule (3.11) is identically zero. For the Feynman rules with the vector photon A_i it is important to note that there are photon polarization vectors ϵ_1 and ϵ_2 needed also, which we will eventually multiply the amplitudes with.

The full di-cluster propagator is defined in Fig. 3.1. In the c.m. frame it is constructed from the bare di-cluster propagator $iD^{(0)}(E, 0)$, Eq. (3.4), as the geometrical series

$$\begin{aligned} iD(E) &= iD^{(0)}(E, 0) + iD^{(0)}(E, 0)i\Sigma(E)iD^{(0)}(E, 0) + \dots \\ &= \frac{i}{\Delta + \nu(E + i\varepsilon) + \Sigma(E)} \end{aligned} \quad (3.13)$$

where we have also introduced the irreducible self-energy Σ . The irreducible self-energy is the bubble-diagram shown in Fig. 3.2, and it is simply given by $(-ig)^2$, from the Feynman rule (3.5), times the Coulomb propagator $\langle 0|G_C(E)|0\rangle$, introduced in Appendix A Eq. (A.1):

$$\Sigma(E) = -g^2 \int \frac{d^3p}{(2\pi)^3} \frac{\psi_{\mathbf{p}}(0)\psi_{\mathbf{p}}^*(0)}{E - \mathbf{p}^2/(2m_R) + i\varepsilon} . \quad (3.14)$$

The integral (3.14) is evaluated to¹

$$\Sigma(E) = g^2 \frac{k_C m_R}{\pi} h_0(\eta) + \Sigma^{\text{div}} . \quad (3.15)$$

Note that the irreducible self-energy is formally infinite, with a divergent part Σ^{div} that is independent of the energy. This is analogous to the renormalization procedure in Chapter 2.1.2. The matching to low-energy elastic scattering parameters and the renormalization is given in Appendix B.1.

¹See Ref. [17] or Appendix B.3.1 for details on the integration.

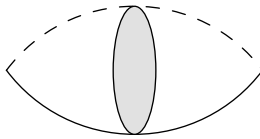


Figure 3.2: The irreducible self-energy diagram for the proton-core pair.

Whenever a bound state observable is to be calculated one needs to include the wavefunction renormalization \mathcal{Z} , such as to normalize the bound-state fields properly. An easy example of such a wavefunction renormalization is for an uncharged S-wave two-body system, with radial bound-state wavefunction $u_0(r) = \exp(-\gamma r)$. The proper normalization can then be seen to be off by a factor of $\sqrt{2\gamma}$, by evaluating the integral $\int_0^\infty dr |u_0(r)|^2$. The wavefunction renormalization for the bound state is given in Eq. (B.7) in terms of the effective range, as

$$\mathcal{Z} = \frac{6\pi k_C}{g^2 m_R^2} \left[-3k_C r_0 + \frac{6k_C^2}{m_R} \frac{d}{dE} h_0(\eta) \right]^{-1} \Big|_{E=-B}. \quad (\text{B.7})$$

Note that for γ/k_C small, the second term in the denominator of Eq. (B.7) can be expanded as $1 + \mathcal{O}(\gamma^2/k_C^2)$. It is instructive to compare the $k_C \gg \gamma$ limit from Eq. (B.10)

$$\mathcal{Z} = \frac{6\pi k_C}{g^2 m_R^2} \frac{1}{1 - 3k_C r_0} + \mathcal{O}\left(\frac{\gamma^2}{k_C^2}\right) \quad (\text{B.10})$$

with the wavefunction renormalization for a one-neutron halo [10]

$$\mathcal{Z}^{\text{neutron halo}} = \frac{2\pi\gamma}{g^2 m_R^2} \frac{1}{1 - \gamma r_0}. \quad (\text{3.16})$$

While the universal low-energy physics for a one-neutron halo is defined by the momentum scale γ , it seems as though the low-energy physics for a one-proton halo, in the limit where $k_C \gg \gamma$, is given in terms of a scale $3k_C$. One can now ask whether such a limit is realized anywhere in Nature. We will consider the $^{17}\text{F}^*$ one-proton halo nucleus for which we have $\gamma/k_C = 0.265$, that is actually small enough for the limit to be qualitatively realized.

For $^{17}\text{F}^*$ we note that there is a fine tuning in the effective range such that the denominator in Eq. (B.7) is very close to zero, that is the wavefunction renormalization \mathcal{Z} is extremely large. This means that all observables that involves the bound state, for example the charge radius and the radiative capture cross section, are enhanced by a large factor \mathcal{Z} . However, due to

Table 3.1: Relevant parameters and scales for the $^{17}\text{F}^*$ system. The effective range r_0 has been obtained from the ANC, either by Ref. [27] or [28].

k_C	γ	r_0	$1/R_{16\text{O}}$	$f = m/M_{\text{tot}}$	Z_c
51.2 MeV	13.6 MeV	~ 1.2 fm	~ 70 MeV	1/17	8

the large value of the Coulomb momentum for this system, $k_C = 51.2$ MeV, the Cluster EFT prediction for the $^{17}\text{F}^*$ charge radius is at a rather expected value anyway, as we will see in Section 3.1.3. The large value for the wavefunction renormalization \mathcal{Z} can also be seen from the fact that the asymptotic normalization coefficient (ANC) for $^{17}\text{F}^*$ is very large (on the order of $80 \text{ fm}^{-1/2}$ [27, 28]).

3.1.2 Fixing parameters

At LO in the Cluster EFT for an S-wave interaction there is only one free parameter. We fix this to the proton separation energy, B , in the form of the binding momentum $\gamma = \sqrt{2m_R B}$ of the system. For $^{17}\text{F}^*$ the binding momentum is $\gamma = 13.6$ MeV [29] and this value will be the only non-trivial input at LO. The other important scale for the $^{17}\text{F}^*$ system is the Coulomb momentum $k_C = 51.2$ MeV. Relevant parameters and scales are summarized in Table 3.1.

At the next order we have an effective range correction coming in through the factor $1/(1 - 3k_C r_0)$, using the approximate form of the wavefunction renormalization (B.10). For a system where the effective range scales naturally as $r_0 \sim 1/k_{\text{hi}}$, this correction would just be given by the first order term in the expansion $1/(1 - 3k_C r_0) = 1 + 3k_C r_0 + \dots$, that is $3k_C r_0 \sim k_{\text{lo}}/k_{\text{hi}}$ times the LO result. However, for $^{17}\text{F}^*$ the effective range is close to $1/(3k_C) = 1.29$ fm, which means that we are very near the pole of the wavefunction renormalization. This means that we must resum the effective range and use the full correction factor $1/(1 - 3k_C r_0)$. One might even argue that one should include the effective range at LO for such a fine-tuned system. Note that even though the effective range is fine-tuned to be close to the pole, it does not scale unnaturally in the sense that it is unnaturally small or large.

If we extract the effective range from the measurement of Ref. [30] we find $r_0 \approx 1.3$ fm, which is very close to the pole position $1/(3k_C)$. Since the correction factor $1/(1 - 3k_C r_0)$ is very sensitive to the exact value of r_0 , the elastic scattering data used must be extremely accurate.

If we instead use an extracted or calculated ANC for the $^{17}\text{F}^*$ state, to

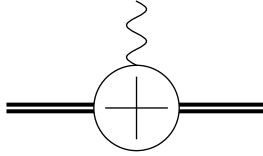


Figure 3.3: A sketch of the general charge form factor diagram. The diagram consists of an incoming and outgoing bound halo state, and a virtual photon leg. The crossed white blob corresponds to the halo-photon interaction and defines the charge form factor of the halo state.

extract the effective range, we will get the correct wavefunction renormalization, since $\mathcal{Z} \propto A^2$, where A is the ANC. Using $A = 77.21 \text{ fm}^{-1/2}$ from Ref. [27], extracted from the radiative capture reaction $^{16}\text{O}(p, \gamma)^{17}\text{F}^*$ using a single-particle model, or the ANC squared $A^2 = 6490 \pm 680 \text{ fm}^{-1}$ from Ref. [28], extracted from the transfer reaction $^{16}\text{O}(^3\text{He}, d)^{17}\text{F}$, we find an effective range $r_0 \approx 1.2 \text{ fm}$. Note that if we use the effective range extracted from Ref. [30], the obtained ANC would be off by an order of magnitude. Therefore, using an ANC as input, one can circumvent the problems due to the fine-tuning. The effective range can be calculated using the ANC formula of Ref. [31]²

$$A^2 = 6k_C \Gamma(1 + k_C/\gamma)^2 \left[-3k_C r_0 + \frac{6k_C^2}{m_R} \frac{d}{dE} h_0(\eta) \right] \Big|_{E=-B}. \quad (3.17)$$

Comparing Eqs. (3.17) and (B.7) it is evident that we can write the wavefunction renormalization in terms of the ANC according to

$$\mathcal{Z} = \frac{\pi}{g^2 m_R^2 \Gamma(1 + k_C/\gamma)^2} A^2. \quad (3.18)$$

3.1.3 The charge form factor

The charge form factor is given in terms of the zeroth component of the electromagnetic four-current J^μ , as

$$F_C(\mathbf{Q}) = \frac{1}{eZ} \langle \mathbf{k}' | J^0 | \mathbf{k} \rangle, \quad (3.19)$$

where $\mathbf{Q} = \mathbf{k}' - \mathbf{k}$ is the momentum transfer. Thus, the charge form factor can be calculated as the interaction of the bound state nucleus with a virtual

²There is a minor error in the formula Eq. (85) of [31]; the $\tilde{C}_{\eta,l}$ should be in the numerator.

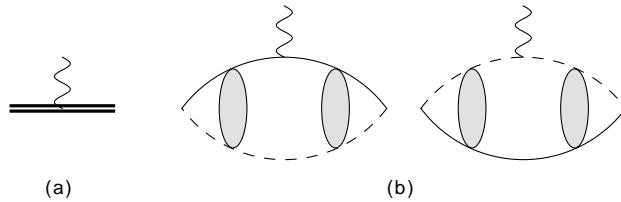


Figure 3.4: The charge form factor diagrams. (a) The tree-level diagram Γ_{tree} , where the virtual photon couples to the halo field, and (b) the loop-diagram $\Gamma_{\text{loop}}(Q)$, where the photon couples to the core and the proton fields, respectively. The loop-diagram depends on the momentum transfer Q , while the tree-level diagram only gives a constant contribution to the charge form factor.

photon in the Breit frame, with energy $\omega = 0$ and momentum \mathbf{Q} . The general form of such a diagram is shown in Fig. 3.3. The crossed blob represents all possible interactions with the external virtual photon leg and the relevant diagrams are given and calculated below. The charge radius r_C is defined by the Q^2 coefficient of the charge form factor according to the expansion

$$F_C(Q) = 1 - \frac{r_C^2}{6} Q^2 + \dots, \quad (3.20)$$

and thus the aim is to calculate the charge form factor to second order in the momentum transfer Q .

Including effective-range corrections there are two charge form factor diagrams for an S-wave interaction, and these are shown in Fig. 3.4. In the following parts of this section we construct these amplitudes and show how they give the charge form factor of the system.

Charge form factor diagrams

The loop-diagram in Fig. 3.4(b), $\Gamma_{\text{loop}}(Q)$, consists of a proton-core bubble, where the external photon line couples to either the core or the proton, with Feynman rules given by Eqs. (3.7) and (3.6), respectively. The shaded blobs denote the Coulomb resummation and they are simply given by two-body Coulomb propagators $\langle \mathbf{p}' | G_C(-B) | \mathbf{p} \rangle$, where the angle brackets are used for momentum space. In total, therefore, we have one interaction vertex between an A_0 photon and either a core or a proton, two contact interaction vertices with Feynman rule given in Eq. (3.5), two Coulomb propagators and three momentum loops to be integrated over. In momentum space the

loop-diagram is therefore given by

$$\begin{aligned} \Gamma_{\text{loop}}(Q) = & g^2 e Z_c \int \frac{d^3 p_1}{(2\pi)^3} \frac{d^3 p_2}{(2\pi)^3} \frac{d^3 p_3}{(2\pi)^3} \langle \mathbf{p}_1 | G_C(-B) | \mathbf{p}_2 + f\mathbf{Q}/2 \rangle \\ & \times \langle \mathbf{p}_2 - f\mathbf{Q}/2 | G_C(-B) | \mathbf{p}_3 \rangle \\ & + [(f \rightarrow 1-f), (Z_c \rightarrow 1)] . \end{aligned} \quad (3.21)$$

Note that in using the two-body Coulomb propagators we have already performed the energy residue integrals; the Coulomb propagators are at the bound state energy $E = -B$. The $[(f \rightarrow 1-f), (Z_c \rightarrow 1)]$ term is due to the fact that the photon can interact with both the core and the proton. In Eq. (3.21) we have introduced the mass ratio $f = m/M_{\text{tot}}$, which is useful in defining the differences in kinematics for the proton and the core. The momentum dependencies in the Coulomb propagators are relative momenta of the proton and the core. For example, in the loop where the photon is attached to the core we define the proton momentum as \mathbf{p}_2 , while the core momentum is $-\mathbf{p}_2 - \mathbf{Q}/2$ before the photon interaction and $-\mathbf{p}_2 + \mathbf{Q}/2$ after. This gives the relative momenta $\mathbf{p}_2 + f\mathbf{Q}/2$ and $\mathbf{p}_2 - f\mathbf{Q}/2$, respectively, using the defining equation (3.12).

Performing a Fourier transform on each of the momentum-space kets and bras, we arrive at the much simpler coordinate-space integral

$$\begin{aligned} \Gamma_{\text{loop}}(Q) = & g^2 e Z_c \int d^3 r (0 | G_C(-B) | \mathbf{r}) \exp(i f \mathbf{Q} \cdot \mathbf{r}) (\mathbf{r} | G_C(-B) | 0) \\ & + [(f \rightarrow 1-f), (Z_c \rightarrow 1)] , \end{aligned} \quad (3.22)$$

where the coordinate space Coulomb propagators must be purely S-wave since they have one end at zero separation. For coordinate space we use round brackets. Using Eq. (A.27) we write these propagators as

$$|(0 | G_C(-B) | \mathbf{r})|^2 = \frac{m_R^2}{(2\pi)^2} \Gamma(1 + k_C/\gamma)^2 \frac{W_{-k_C/\gamma, 1/2}(2\gamma r)^2}{r^2} , \quad (3.23)$$

where W is the Whittaker-W function. The integral (3.22) is now straightforward to evaluate numerically.

The tree-level diagram in Fig. 3.4(a) Γ_{tree} is from a two-body current operator, and it enters with an effective-range correction. The diagram is simply

$$\Gamma_{\text{tree}} = \nu e (Z_c + 1) , \quad (3.24)$$

which is a constant.

Summing the contributions from the diagrams, Eqs. (3.22) and (3.24), we can arrive at the observable $\langle \mathbf{k}' | J^0 | \mathbf{k} \rangle$ in Eq. (3.19); we only need to normalize

the diagrams properly first. This is done with one square root of the LSZ residue factor, Eq. (B.7), for each bound-state end of the diagrams in Fig. 3.4. The charge form factor is therefore given in terms of the diagrams Eqs. (3.22) and (3.24) and in total one power of the LSZ residue \mathcal{Z} as

$$F_C(Q) = \frac{\mathcal{Z}}{e(Z_c + 1)} (\Gamma_{\text{loop}}(Q) + \Gamma_{\text{tree}} + \dots) \quad (3.25)$$

where the dots refer to higher-order diagrams that we do not consider here.

Normalization of the charge form factor

At zero momentum transfer ($Q = 0$) the charge form factor must be equal to one, as is evident from Eq. (3.20). In this section we show that this is indeed the case, using Eq. (3.25) for the charge form factor.

At $Q = 0$ Eq. (3.22) reduces to

$$\Gamma_{\text{loop}}(0) = g^2 e(Z_c + 1) \int d^3r (0|G_C(-B)|\mathbf{r})(\mathbf{r}|G_C(-B)|0) . \quad (3.26)$$

Using the spectral representation of the Coulomb Green's function

$$(0|G_C(E)|\mathbf{r}) = \int \frac{d^3p}{(2\pi)^3} \frac{\psi_{\mathbf{p}}(0)\psi_{\mathbf{p}}^*(\mathbf{r})}{E - \mathbf{p}^2/(2m_R) + i\varepsilon} , \quad (3.27)$$

and orthonormality of the Coulomb wave functions

$$\int d^3r \psi_{\mathbf{p}}^*(\mathbf{r})\psi_{\mathbf{p}'}(\mathbf{r}) = (2\pi)^3 \delta^{(3)}(\mathbf{p} - \mathbf{p}') , \quad (3.28)$$

Eq. (3.26) is simply

$$\begin{aligned} \Gamma_{\text{loop}}(0) &= g^2 e(Z_c + 1) \int \frac{d^3p}{(2\pi)^3} \frac{\psi_{\mathbf{p}}(0)\psi_{\mathbf{p}}^*(0)}{(-B - \mathbf{p}^2/(2m_R) + i\varepsilon)^2} \\ &= e(Z_c + 1)\Sigma'(-B) , \end{aligned} \quad (3.29)$$

where we used Eq. (3.14) for the irreducible self-energy in the last step.

The form factor (3.25) at $Q = 0$ is now given by, using Eqs. (B.6), (3.24) and (3.29),

$$\begin{aligned} F_C(0) &= \frac{1}{\nu + \Sigma'(-B)} \frac{1}{e(Z_c + 1)} (\Gamma_{\text{tree}}^0 + \Gamma_{\text{loop}}^0(0)) \\ &= \frac{1}{\nu + \Sigma'(-B)} (\nu + \Sigma'(-B)) \\ &= 1 , \end{aligned} \quad (3.30)$$

which demonstrates proper normalization.

The charge radius

We have shown that the charge form factor is properly normalized and it is straightforward to show that the order Q term is identically zero, since it will integrate to zero in Eq. (3.22). In obtaining the charge radius, we can therefore focus completely on the order Q^2 term.

The charge radius r_C is defined by the Q^2 coefficient of the charge form factor, according to Eq. (3.20), $F_C(Q) = 1 - \frac{r_C^2}{6}Q^2 + \dots$. Therefore, using Eq. (3.25), the charge radius is given by

$$r_C^2 = -\frac{3}{e(Z_c + 1)} Z \Gamma''_{\text{loop}}(0), \quad (3.31)$$

where the prime denotes a derivative with respect to the momentum Q . Thus, by evaluating the integral (3.22) numerically and inserting the result into Eq. (3.31), the Cluster EFT charge radius result for a given system can be obtained.

The charge radius of $^{17}\text{F}^*$

As an application of these Cluster EFT results we use parameters for the $^{17}\text{F}^*$ one-proton halo nucleus. The values used as input are the binding momentum $\gamma = 13.6$ MeV and the extracted ANC from Huang et al. [27], $A_H = 77.21 \text{ fm}^{-1/2}$, and from Gagliardi et al. [28], $A_G = 80.6 \text{ fm}^{-1/2}$ (we use only the central value). As we discussed in Section 3.1.1, the effective range is fine-tuned to be very close to the pole in the wavefunction renormalization, and therefore we choose to include the effective range already at LO. Therefore, the results that we present is at LO, but with the effective-range correction included. With the two different $^{17}\text{F}^*$ inputs we find the charge radius

$$r_C = \begin{cases} 2.12 \text{ fm} & \text{ANC from Huang et al. [27]} \\ 2.24 \text{ fm} & \text{ANC from Gagliardi et al. [28]} \end{cases}. \quad (3.32)$$

The LO Cluster EFT prediction for the charge radius of $^{17}\text{F}^*$ is very small and it is difficult to do a good estimate of the EFT error, due to the fine-tuning in the effective range. Using the size of the ^{16}O core, corresponding to ~ 70 MeV, as a breakdown scale we have an expected EFT error of 20% on the charge radius squared. However, such an error estimate is probably too optimistic for this system.

There exists a short-range operator $d^\dagger \nabla^2 A_0 d$, that will contribute to the charge radius at the next order in the power counting. As of now, we have no means to fit such an operator to anything but the charge radius itself. Thus, it might be the case that a higher-order calculation of the $^{17}\text{F}^*$ charge

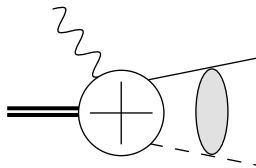


Figure 3.5: Sketch of the general radiative capture diagram. The diagram consists of an incoming proton-core pair, which is given by a Coulomb wave function, an outgoing bound halo state and an outgoing real photon. The crossed white blob indicates all the possible relevant interactions. The direction of time is from right to left.

radius is permanently unavailable using two-body Cluster EFT. Luckily, the situation looks much more optimistic for other observables.

3.1.4 Radiative capture and the astrophysical S-factor

Radiative nucleon capture is the capture of a nucleon on a core, while emitting a photon. There also exist radiative capture of clusters of nucleons, for example ${}^3\text{He}({}^4\text{He}, \gamma){}^7\text{Be}$, and the formalism we present below can straightforwardly be extended to include these. When the captured nucleon is a proton, the cross section is exponentially suppressed at low energies, due to the repulsive Coulomb barrier; the proton must tunnel through this barrier. Therefore, this process is very difficult to measure experimentally. However, many of the important reactions in the nucleosynthesis are radiative capture processes of charged particles and therefore, if we wish to understand how the elements in Nature were created, we need to consider these processes.

The fact that these reactions are so hard to measure only makes them even more interesting from the viewpoint of a nuclear theorist. Accurate cross-section predictions is important input for the nucleosynthesis modeling and in the solar-fusion processes these reactions occur at energies around 10 keV. Therefore, the effort of pinning down the exact cross sections for radiative capture reactions is a joint venture between nuclear experiment and theory, where experiments can only measure accurately down to some hundred keV and theory can provide good models for extrapolation of the data down to threshold.

The conventional way of presenting radiative proton capture cross sections is through the astrophysical S-factor

$$S(E) = E \exp(2\pi\eta)\sigma_{\text{tot}}(E) , \quad (3.33)$$

where E is the c.m. energy. The S-factor is defined in such a way that the exponential Coulomb repulsion has been removed, and as such the S-factor

is a much more convenient object than the exponentially suppressed cross section $\sigma_{\text{tot}}(E)$.

In Fig. 3.5 a sketch of a general capture diagram is shown. On the right side of the diagram is the incoming proton-core pair, which interacts to all orders with the Coulomb interaction. This incoming proton-core pair has a relative momentum \mathbf{p} and energy $E = \mathbf{p}^2/(2m_R)$, and can be described by a Coulomb wavefunction $\psi_{\mathbf{p}}$. To the left are the outgoing halo field with momentum $-\mathbf{k}$, represented by the double-line, and the real photon with four momentum (ω, \mathbf{k}) , in the zero-momentum frame. Energy conservation implies that $\omega = -M_{\text{tot}} + \sqrt{M_{\text{tot}}^2 + 2M_{\text{tot}}(E + B)}$, where B is the binding energy or one-proton separation energy. Considering energies much smaller than the total mass M_{tot} we find $\omega \approx B + E$. The crossed white blob denotes all the possible interactions that can take place in the process, and it is these interactions that are organized in a power counting in the EFT.

In Appendix B.2 the radiative capture amplitude, up to NLO, is derived. The resulting amplitude, Eq. (B.12), is given by

$$\begin{aligned} \mathcal{A} = & -ig\sqrt{\mathcal{Z}}\frac{eZ_c f}{m_R} \int d^3r G_C^{(0)}(-B; 0, \rho) \exp(-if\mathbf{k} \cdot \mathbf{r}) \nabla \psi_{\mathbf{p}}(\mathbf{r}) \\ & - [(f \rightarrow 1 - f), (Z_c \rightarrow 1)] . \end{aligned} \quad (\text{B.12})$$

One can understand Eq. (B.12) in terms of standard quantum mechanics. At the far right there is an incoming Coulomb wavefunction $\psi_{\mathbf{p}}(\mathbf{r})$. In the middle we have the vector current operator $\frac{eZ_c f}{m_R} \exp(-if\mathbf{k} \cdot \mathbf{r}) \nabla$, corresponding to the interaction between the core and the vector photon. And at the far left in the integrand is the bound state wavefunction $G_C^{(0)}(-B; 0, \rho) \propto W_{-k_C/\gamma, 1/2}(2\gamma r)/r$, given in Eq. (A.27). Due to the presence of one bound-state field, there is a wavefunction renormalization $\sqrt{\mathcal{Z}}$ present. Of course the photon can couple to both the core and the proton and hence the $- [(f \rightarrow 1 - f), (Z_c \rightarrow 1)]$ piece, where the minus sign can be traced back to the Feynman rule for the interaction with the vector photon.

By multiplying the amplitude Eq. (B.12) with the photon polarization vectors ϵ_i (note that both \mathcal{A} and ϵ_i are vector quantities) and squaring, we arrive at the differential cross section, Eq. (B.15)

$$\frac{d\sigma}{d\Omega} = \frac{m_R \omega}{8\pi^2 p} \sum_i |\epsilon_i \cdot \mathcal{A}|^2 , \quad (\text{B.15})$$

where in Coulomb gauge we have the Ward identity

$$\epsilon_i \cdot \mathbf{k} = 0 . \quad (\text{3.34})$$

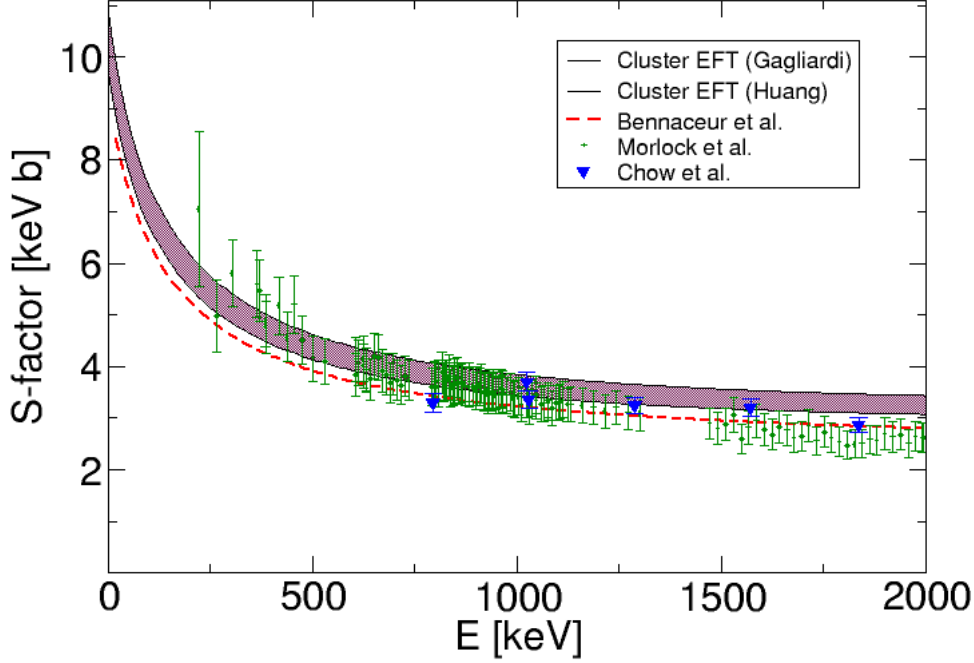


Figure 3.6: The astrophysical S-factor for $^{16}\text{O}(p, \gamma)^{17}\text{F}^*$, plotted as a function of the center-of-mass energy E . The dashed red curve is the SMEC result by Bennaceur et al. [32], the green dots are the measurements by Morlock et al. [33] and the blue triangles are the measurements by Chow et al. [34]. The purple band, between the two solid black lines, is the Cluster EFT result. The upper solid black line was generated using the ANC by Gagliardi et al. [28] and the lower dashed black line by using the ANC by Huang et al. [27].

Once Eq. (B.12) has been multiplied with the photon polarization vectors the

angular integrals are easily evaluated and we arrive at the integral (B.14),

$$\begin{aligned} \sum_i |\epsilon_i \cdot \mathcal{A}|^2 = & \left| \sqrt{Z} \sin \theta (\cos \phi + \sin \phi) \frac{4\pi g e Z_c f \exp(i\sigma_1)}{m_{\text{R}p}} \right. \\ & \times \int dr G_{\text{C}}^{(0)}(-B; 0, \rho) j_0(f\omega r) \frac{\partial}{\partial r} [r F_1(k_{\text{C}}/p, pr)] \\ & \left. - [(f \rightarrow 1 - f), (Z_c \rightarrow 1)] \right|^2, \end{aligned} \quad (\text{B.14})$$

which can be calculated numerically. The P-wave Coulomb wavefunction, F_1 , is introduced in Appendix A. Note that the result (B.14) depends on the angles ϕ and θ . These are the angles that are integrated over when going from the differential cross section (B.15) to the total cross section.

As an application of the Cluster EFT result (B.14) we use the $^{17}\text{F}^*$ halo system. The resulting Cluster EFT S-factor is shown in Fig. 3.6, together with measured data [33, 34] and a phenomenological calculation using a shell model embedded in the continuum (SMEC) by Ref. [32]. The lower bound of the Cluster EFT band corresponds to the ANC extracted by Huang et al. [27] and the upper bound is for the ANC extracted from the transfer reaction $^{16}\text{O}(^3\text{He}, d)^{17}\text{F}$, by Gagliardi et al. [28]. At low energies, the Cluster EFT result agrees well with both the SMEC result and the data. However, at higher energies the result deviates slightly, which is expected since there are higher-order operators that have not been included. The obtained threshold value for the S-factor of $^{17}\text{F}^*$ is

$$S(0) = \begin{cases} 9.7 \text{ keV b} & \text{ANC from Huang et al. [27]} \\ (10.9 \pm 1.1) \text{ keV b} & \text{ANC from Gagliardi et al. [28]} \end{cases}, \quad (3.35)$$

where the shown error is due to the error on the extracted ANC. Note that no error is presented on the ANC in Ref. [27].

It would be interesting to use low-energy elastic scattering data, in addition to the ANC input, to constrain the S-factor. However, since the effective range is very close to the pole position it would have to be measured to the third (fourth) digit for the resulting S-factor error to be about 10% (1%). For such accuracies the shape parameter is needed, and possibly also higher-order terms in the ERE.

3.2 P-wave one-proton halo nuclei – The ${}^8\text{B}$ nucleus

In this section we continue by presenting formalism and results for a one-proton halo nucleus bound by a P-wave interaction. The interaction being of P-wave nature implies that two parameters are needed at LO to renormalize the theory. We show results for the charge radius of ${}^8\text{B}$ and the radiative proton capture cross section for ${}^7\text{Be}(p, \gamma){}^8\text{B}$. A particularly interesting result is the demonstration of a correlation between the charge radius and the threshold S-factor. This section is based on work presented in Paper 2.

3.2.1 Interactions

The main reason, in this thesis, for studying P-wave interactions in Cluster EFT is the one-proton halo nucleus ${}^8\text{B}$. It consists of a ${}^7\text{Be}$ core and a proton being dominantly in a relative P-wave. The ground-state core of ${}^7\text{Be}$ has spin and parity $3/2^-$ and this state together with the proton, of spin $1/2^+$, then define two spin channels $S = 1, 2$. Both of these channels contribute to the ${}^8\text{B}(2^+)$ state via a P-wave interaction. In addition, there is an excited $1/2^-$ state of ${}^7\text{Be}$, at $E_* = 0.429$ MeV, which can combine in a P-wave with a proton to form the ${}^8\text{B}(2^+)$ state if the spin channel is $S = 1$. Comparing this system with the simpler case of the S-wave one-proton halo nucleus ${}^{17}\text{F}^*$, where only one channel was present, we note that the ${}^8\text{B}$ halo is a more involved system both counting the number of spin-coupled channels and the increased complexity due to the P-wave nature of the interaction.

The reason why the P-wave interaction introduces difficulties is due to the need for two independent renormalizations already at LO. This difficulty comes from the fact that the LO Dirac delta contact interaction enters with one power of the relative momentum of the proton-core pair. This momentum dependence of the interaction vertex makes the irreducible self-energy, Eq. (B.33), have an additional divergence compared to the S-wave case, Eq. (3.15). See Appendix B.3 or Ref. [4] for a full derivation of these renormalization issues.

For a P-wave interaction, the Coulomb-modified ERE is given by Eq. (A.13) with $l = 1$. However, the elastic scattering process of a proton and a ${}^7\text{Be}$ core has a contribution from the core excitation ${}^7\text{Be}^*$ and therefore, for the case at hand, we have the ERE (B.42)

$$k^3 C(1, \eta)^2 (\cot \delta_1 - i) + 2k_C h_1(\eta) + \frac{g_*^2}{g^2} 2k_C h_1(\eta_*) = -\frac{1}{a_1} + \frac{1}{2} r_1 k^2 + \dots \quad (\text{B.42})$$

In Eq. (B.42) we have introduced two new parameters: the ratio between the interaction vertices of proton- ${}^7\text{Be}^*$ and proton- ${}^7\text{Be}$, g_*/g , and the Coulomb parameter $\eta_* = k_C/k_*$, with $k_* = \sqrt{k^2 - 2m_R E_*}$. The effective range r_1 and the ratio g_*/g we shall fit to calculated and measured ANCs in Section 3.2.2. Details on how the ERE (B.42) is obtained from the interactions of the field theory can be found in Appendix B.3.

The Lagrangian for a system consisting of a proton interacting with a spin-3/2 core state and a spin-1/2 excited-core state, in a relative P-wave with total spin $J = 2$, is given by

$$\begin{aligned}
\mathcal{L} = & p_\sigma^\dagger \left(iD_t + \frac{\mathbf{D}^2}{2m} \right) p_\sigma + c_a^\dagger \left(iD_t + \frac{\mathbf{D}^2}{2M} \right) c_a + \tilde{c}_\sigma^\dagger \left(iD_t + \frac{\mathbf{D}^2}{2M} - E_* \right) \tilde{c}_\sigma \\
& + d_\alpha^\dagger \left[\Delta + \nu \left(iD_t + \frac{\mathbf{D}^2}{2M_{\text{tot}}} \right) \right] d_\alpha \\
& - g_1 \left[d_\alpha^\dagger \mathcal{C}_{ji}^\alpha \mathcal{C}_{a\sigma}^j c_a \left((1-f)i\vec{D}_i - fi\overleftarrow{D}_i \right) p_\sigma + \text{h.c.} \right] \\
& - g_2 \left[d_\alpha^\dagger \mathcal{C}_{\beta i}^\alpha \mathcal{C}_{a\sigma}^\beta c_a \left((1-f)i\vec{D}_i - fi\overleftarrow{D}_i \right) p_\sigma + \text{h.c.} \right] \\
& - g_* \left[d_\alpha^\dagger \mathcal{C}_{ji}^\alpha \mathcal{C}_{\chi\sigma}^j \tilde{c}_\chi \left((1-f)i\vec{D}_i - fi\overleftarrow{D}_i \right) p_\sigma + \text{h.c.} \right] \\
& + \dots
\end{aligned} \tag{3.36}$$

In this Lagrangian, the proton field is denoted by p_σ , the ground state core field by c_a , the excited state core field by \tilde{c}_σ and the spin-2⁺ dicluster field by d_α . The core fields have mass M and charge eZ_c , the proton field has mass m and charge e , and the dicluster field has mass $M_{\text{tot}} = M + m$ and charge $e(Z_c + 1)$. Note also that the excited-state core field has excitation energy E_* . The mass ratio f is defined as $f = m/M_{\text{tot}}$ and the factors of $(1-f)$ and f in the interaction part of the Lagrangian (3.36) make sure that it is Galilean invariant. The interaction vertices for the ground-state core field and the proton have coupling strengths g_1 and g_2 for the two spin channels $S = 1, 2$. To the order that we consider, these couplings always appear in the combination $g^2 = g_1^2 + g_2^2$. The interaction vertex for the excited-state core field and the proton have coupling strength g_* . With the Clebsch-Gordan coefficients \mathcal{C} the different interaction channels are defined, with indices according to $\alpha, \beta = -2, -1, 0, 1, 2$, $a = -3/2, -1/2, 1/2, 3/2$, $i, j, k = -1, 0, 1$, and $\sigma, \chi = -1/2, 1/2$. The covariant derivatives are given by $D_\mu = \partial_\mu + ie\hat{Q}A_\mu$. The dots refer to higher-order terms that we do not include.

The P-wave interaction vertices for the ground state core-proton-dicluster interactions are

$$ig_1 \mathcal{C}_{ji}^\alpha \mathcal{C}_{a\sigma}^j k_i, \tag{3.37}$$

for the $S = 1$ channel, and

$$ig_2 \mathcal{C}_{\beta i}^\alpha \mathcal{C}_{a\sigma}^\beta k_i, \quad (3.38)$$

for the $S = 2$ channel, and for the excited state core field

$$ig_* \mathcal{C}_{ji}^\alpha \mathcal{C}_{\chi\sigma}^j k_i, \quad (3.39)$$

where \mathbf{k} is the relative momentum of the proton-core pair. Therefore, in all loop-diagrams that we consider for the P-wave bound state there will be additional powers of the loop-momentum \mathbf{k} . We consider the most basic P-wave loop-integrals in Appendix B.3. The Feynman rules for the A_0 and the A_i photon interaction with the proton, ground- and excited-state core and dicluster fields are analogous to the rules given in Section 3.1.1. However, for the P-wave interaction at hand, there is also an interaction vertex where an A_i photon is attached to a proton-core-dicluster vertex. This vertex exists for both the ground- and excited-state core, but for the purpose of obtaining the results presented here we only need the one with the ground-state core field. The Feynman rules for this vertex is, for $S = 1$,

$$ig_1 \mathcal{C}_{ji}^\alpha \mathcal{C}_{a\sigma}^j e[1 - f(Z_c + 1)] \quad (3.40)$$

and for $S = 2$

$$ig_2 \mathcal{C}_{\beta i}^\alpha \mathcal{C}_{a\sigma}^\beta e[1 - f(Z_c + 1)]. \quad (3.41)$$

The bare dicluster propagator for P-wave interactions in the c.m. frame is given by

$$iD^{(0)}(E) = \frac{i}{\Delta + \nu(E + i\varepsilon)}, \quad (3.42)$$

taking the inverse of the kinetic term in the Lagrangian Eq. (3.36). The full dicluster propagator is obtained by dressing the bare propagator Eq. (3.42) by proton-core and proton-excited core loops, that is by including the irreducible self-energies of the proton-core and proton-excited core systems, analogous to the procedure in Chapter 3.1.1. The construction of these irreducible self-energies is given in Appendix B.3. The resulting full dicluster propagator is

$$iD(E) = \frac{i}{\Delta + \nu(E + i\varepsilon) + \Sigma(E) + \Sigma_*(E)}. \quad (3.43)$$

One can understand the sum of the irreducible self-energies $\Sigma(E) + \Sigma_*(E)$ in the denominator by the fact that the propagation of the dicluster will have contributions from both the ground- and the excited-state core fields. Even higher-energy states would also contribute, had we not excluded these from the EFT. That is, these higher modes are considered short-range physics and are implicitly included in the parameters of the EFT. Note that the total

Table 3.2: Relevant parameters and scales for the ${}^8\text{B}$ system.

k_{C}	γ	γ_*	r_1
26.79 MeV	14.97 MeV	30.39	$\sim 60\text{--}70$ MeV
k_{α}	$1/R\tau_{\text{Be}}$	$f = m/M_{\text{tot}}$	Z_{c}
50.86	74.55 MeV	1/8	4

irreducible self-energy $\Sigma(E) + \Sigma_*(E)$ for the P-wave interaction has two independent divergences, compared to only one for the S-wave interaction, and therefore two parameters are needed at LO to renormalize the interaction. This is independent of the fact that we have one irreducible self-energy per core field.

The wavefunction renormalization of the P-wave bound state ${}^8\text{B}$ system is given in Eq. (B.47) as

$$\mathcal{Z} = \frac{6\pi}{g^2 m_{\text{R}}^2} \left[r_1 - \frac{2k_{\text{C}}}{m_{\text{R}}} \frac{\text{d}}{\text{d}E} \left(h_1(\eta) + \frac{g_*^2}{g^2} h_1(\eta_*) \right) \right]^{-1} \Big|_{E=-B}. \quad (\text{B.47})$$

It is evident that both the ground and excited state of the ${}^7\text{Be}$ core contribute to the bound-state properties of ${}^8\text{B}$, through the $h_1(\eta)$ and $\frac{g_*^2}{g^2} h_1(\eta_*)$ pieces. When we match to ANCs in Section 3.2.2, we will fix both the effective range r_1 and the excited-to-bound state interaction strength ratio g_*/g by matching to the ANCs relevant for the ${}^8\text{B}$ system. In terms of these ANCs the wavefunction renormalization can be written as

$$\mathcal{Z} = - \frac{3\pi}{g^2 m_{\text{R}}^2 \gamma^2 \Gamma(2 + k_{\text{C}}/\gamma)^2} (A_1^2 + A_2^2) \quad (3.44)$$

$$\mathcal{Z} = - \frac{3\pi}{g_*^2 m_{\text{R}}^2 \gamma_*^2 \Gamma(2 + k_{\text{C}}/\gamma_*)^2} A_*^2, \quad (3.45)$$

combining Eq. (B.47) and the ANC formula in Eq. (85) of Ref. [31]. In Eqs. (3.44) and (3.45), A_1 (A_2) is the ANC for the proton and the ground-state core in the $S = 1$ ($S = 2$) channel and A_* is the ANC for the proton and excited-state core in the $S = 1$ channel.

3.2.2 Fixing parameters

In this section we will discuss how to extract parameters from ANCs. We will use two different field theories for the P-wave system under consideration: (i)

A field theory with only the ground-state core included and (ii) a field theory where the excited-state core is also included. Therefore, in the ground-state only theory the breakdown scale is given by the excited-state energy.

For the P-wave system at hand, we need to fix at least two parameters at LO to be able to make predictions, for example the binding momentum and the effective range. Thus, if we only include the ground state of the core in the field theory we would need to fit the effective range to, for example, low-energy elastic scattering data or to an extracted ANC for the bound system, consisting of a proton and a ground-state core. If the excited-core field is also included in the field theory, then an additional parameter needs to be fixed. This parameter is related to the relative importance of the ground- and excited-state core fields, that is in what proportions these fields appear in the halo state. We choose to work with the binding momentum γ of the halo nucleus, the $J = 2^+$ effective range r_1 , and the ratio of the interaction strengths g_*/g as our parameters.

The binding momentum is trivially extracted from the one-proton separation energy B , as $\gamma = \sqrt{2m_{\text{R}}B}$. The two remaining parameters can be fitted to the ground-state core field ANCs, A_1 and A_2 , calculated by (i) Nollett and Wiringa [35], (ii) Navrátil et al. [36] and measured by (iii) Tabacaru et al. [37] and the excited state core field ANC A_* calculated by Zhang et al. [22]. The A_* ANC is also a crucial input if the excited core is to be included in the field theory. The ground-state ANCs, A_1 and A_2 , are for the $S = 1$ and $S = 2$ spin channels, respectively, and the excited-state ANC, A_* , is for the $S = 1$ spin channel. These ANCs are given in Table 3.3.

For the field theory with both the ground- and excited-state core fields included the breakdown scale k_{hi} is defined by the α -threshold at $k_\alpha = 50.86$ MeV. There is also a low-lying 1^+ resonance in ${}^8\text{B}$ at $E_{\text{res}} = 0.77$ MeV, but this state does not contribute to the charge form factor of the ${}^8\text{B}$ ground state and only contributes to the radiative capture process ${}^7\text{Be}(p, \gamma){}^8\text{B}$ for a narrow energy region around E_{res} . The estimate for the EFT error is therefore $k_{\text{lo}}/k_{\text{hi}} \sim \gamma/k_\alpha = 0.29$. For the field theory with only the ground-state core field included the high-momentum scale is defined by the energy of the core excited state $\sqrt{2m_{\text{R}}E_*} = 26.4$ MeV, giving the expansion parameter $k_{\text{lo}}/\tilde{k}_{\text{hi}} \sim 0.57$.

Using the ANC-formula in [31]³, and generalizing it to our case with two

³There is a minor error in the formula Eq. (85) of [31]: the $\tilde{C}_{\eta,l}$ should be in the numerator.

Table 3.3: Asymptotic Normalization Coefficients (ANCs) calculated by Nollett and Wiringa [35] and Zhang *et al.* [22] (denoted “Nollett”), by Navrátil *et al.* [36], and extracted from a proton-transfer reaction by Tabacaru *et al.* [37]. The ANCs are given in fm^{-1/2} for the two spin-channels $S = 1, 2$ (A_1, A_2) and for the $S = 1$ channel with an excited core (A_*).

Ref.	A_1	A_2	A_*
“Nollett” [35], [22]	-0.315(19)	-0.662(19)	0.3485(51)
“Navrátil” [36]	-0.294	-0.650	-
“Tabacaru” [37]	0.294(45)	0.615(45)	-

core fields, we have for P-waves

$$A_1^2 + A_2^2 = \frac{2\gamma^2\Gamma(2 + k_C/\gamma)^2}{-r_1 + \frac{2k_C}{m_R} \frac{d}{dE} \left(h_1(\eta) + \frac{g_*^2}{g^2} h_1(\eta_*) \right)} \Bigg|_{E=-B} \quad (3.46)$$

and

$$A_*^2 = \frac{2\gamma_*^2\Gamma(2 + k_C/\gamma_*)^2}{-\frac{g^2}{g_*^2}r_1 + \frac{2k_C}{m_R} \frac{d}{dE} \left(\frac{g^2}{g_*^2} h_1(\eta) + h_1(\eta_*) \right)} \Bigg|_{E=-B} . \quad (3.47)$$

Note that these ANC formulas are for a field theory with both the ground- and excited-state core fields included. For a field theory with only the ground-state core field we would only have a single ANC formula

$$A_1^2 + A_2^2 = \frac{2\gamma^2\Gamma(2 + k_C/\gamma)^2}{-\tilde{r}_1 + \frac{2k_C}{m_R} \frac{d}{dE} h_1(\eta)} \Bigg|_{E=-B} , \quad (3.48)$$

where the effective range r_1 for the full field theory, and \tilde{r}_1 for the ground-state only field theory are different. Of course, Nature has an exact value for the effective range and r_1 and \tilde{r}_1 are approximations of the exact value, with EFT errors of the order k_{lo}/k_{hi} . Note that k_{hi} is larger for the field theory that does include the excited core and therefore r_1 is likely to be a better approximation to the true effective range than the ground-state-only result \tilde{r}_1 .

Using the full field theory with both the ground- and excited-state core fields, the resulting effective range is,

$$r_1 = \begin{cases} (60 \pm 4) \text{ MeV} & \text{(Nollett ANCs)} \\ 63 \text{ MeV} & \text{(Navrátil ANCs)} \\ (69 \pm 13) \text{ MeV} & \text{(Tabararu ANCs)} \end{cases} . \quad (3.49)$$

Note that no error is presented for the ANC's computed by Navrátil et al. [36]. If the simpler field theory is used instead, with only the ground-state core field, and with the central value of the ‘‘Nollett’’ ANC's, the resulting effective range is $\tilde{r}_1 = 56$ MeV, that is about 7% smaller. In this way, by including more physics successively, one can see convergence towards the physical value of the observable. Note that the effective range result presented in Eq. (3.49) is a prediction, with an estimated error $k_{\text{lo}}/k_{\text{hi}} \sim 29\%$.

The effective range scales naturally with the high momentum scale $r_1 \sim k_{\text{hi}}$. Comparing to the $^{17}\text{F}^*$ S-wave one-proton halo case, where the system is fine-tuned, we instead have that the pole is approximately determined by $1/r_1$; since r_1 is very large compared to the rest of the terms in the denominators of Eqs. (3.46), (3.47) and (3.48). The observation that the ^8B one-proton halo system is more natural than the $^{17}\text{F}^*$ system is connected to the fact that for ^8B we have $k_C \sim \gamma$, while for $^{17}\text{F}^*$ we have $k_C \gg \gamma$.

3.2.3 The charge form factor

As was discussed in the beginning of Chapter 3.1.3 the charge form factor is given by the interaction of the system with an off-shell A_0 photon in the Breit frame, that is Eq. (3.19). The charge form factor diagrams are given and calculated in Appendix B.4. The goal of this section is to calculate the charge radius r_C , defined by Eq. (3.20).

In Appendix B.4 the charge form factor loop-diagram Γ_{loop} is given and simplified, and the resulting integral is

$$\begin{aligned} \Gamma_{\text{loop}}(Q) = & -i3g^2eZ_c \int d^3r \exp(if\mathbf{Q} \cdot \mathbf{r}) \left| \lim_{r' \rightarrow 0} \left(\frac{G_C^{(1)}(-B; r', r)}{r'} \right) \right|^2 \\ & -i3g_*^2eZ_c \int d^3r \exp(if\mathbf{Q} \cdot \mathbf{r}) \left| \lim_{r' \rightarrow 0} \left(\frac{G_C^{(1)}(-B - E_*; r', r)}{r'} \right) \right|^2 \\ & + \left[(f \rightarrow 1 - f), (Z_c \rightarrow 1) \right], \end{aligned} \quad (3.50)$$

combining Eqs. (B.49) and (B.50). In Eq. (3.50) both the ground and excited state core field contributions are explicitly visible, as the first row is only from the ground-state core and the second row from the excited-state core field. The integrals (3.50) are solved numerically using the partial-wave projected Coulomb Green's function Eq. (A.28). The charge radius is now given by numerical integration of the order Q^2 part of Eq. (3.50), according to Eq. (B.58)

$$r_C^2 = -3 \frac{\mathcal{Z}}{e(Z_c + 1)} \Gamma''_{\text{loop}}, \quad (B.58)$$

Apart from the resulting charge radius it is also important that the Cluster EFT formalism gives the correct normalization of the charge form factor at $Q = 0$, that is $F_C(0) = 1$. This is indeed the case, as shown in Appendix B.4.2.

We apply the resulting Eqs. (3.50) and (B.58), together with the partial-wave projected Coulomb Green's function (A.28), on the one-proton halo nucleus ${}^8\text{B}$. As was discussed above, the ${}^7\text{Be}$ core has an excited state only 0.429 MeV above the ground state and therefore we use a field theory where both the ground- and excited-state core fields are included. This is the reason why the loop-integrals (3.50) was derived using both of these fields. However, we may remove the excited-state core field at any time, by setting the coupling strength g_* to zero. The reason why we want to do this is because we wish to see the convergence of the observable charge radius of ${}^8\text{B}$, with respect to the included physics.

The resulting charge radius of ${}^8\text{B}$ is

$$r_C = \begin{cases} (2.56 \pm 0.08) \text{ fm} & \text{(Nollett ANCs)} \\ 2.50 \text{ fm} & \text{(Navrátil ANCs)} \\ (2.41 \pm 0.18) \text{ fm} & \text{(Tabacaru ANCs)} \end{cases}, \quad (3.51)$$

where the ANCs of Nollett and Wiringa [35] (Nollett ANCs), Navrátil et al. [36] (Navrátil ANCs) and measured by Tabacaru et al. [37] (Tabacaru ANCs) have been used as input. The excited-state core field ANC A_* calculated by Zhang et al. [22] has been used for all three results in Eq. (3.51). The binding momentum $\gamma = 14.97$ MeV and the excited state energy $E_* = 0.429$ MeV has also been used as input. The errors given in Eq. (3.51) are due to the errors of the input ANCs.

If the simpler field theory is used, with only the ground-state core field and a proton, then the LO Cluster EFT result for the ${}^8\text{B}$ charge radius is smaller than for the full field theory result. The expected EFT error of the charge radius squared is of order $k_{\text{lo}}/\tilde{k}_{\text{hi}} \sim 57\%$, which propagates to an error of 25% on the charge radius. Using the central values of the Nollett ANCs for the ground-state only and the full field theory, the resulting charge radius of ${}^8\text{B}$ is

$$r_C = \begin{cases} (2.32 \pm 0.58(\text{EFT})) \text{ fm} & \text{, only ground state} \\ (2.56 \pm 0.35(\text{EFT})) \text{ fm} & \text{, ground and excited state} \end{cases}. \quad (3.52)$$

These results clearly demonstrate the convergence of the charge radius, with respect to the inclusion of more physics. This convergence is not due to higher-order calculations. However, it is quite similar since a higher-order calculation would imply the implicit inclusion of more short-range physics.

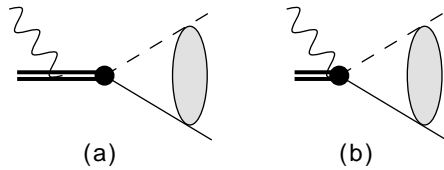


Figure 3.7: Radiative capture diagram that is present for states bound due to a P-wave interaction.

At NLO in the EFT expansion there is a short-range operator $d^\dagger \nabla^2 A_0 d$, corresponding to a two-body current, and as of now we have no means to fit the coefficient of this operator to anything but the charge radius. Therefore we are currently limited to a LO calculation only. This restriction is due to the choice of degrees-of-freedom in our model and it implies that any cluster model should have a minimum error given by this short-range operator.

3.2.4 Radiative capture

In this section we will give results for the radiative capture cross section to a one-proton halo nucleus, where the constituent particles are bound due to a P-wave interaction. We exemplify the formalism by showing results for capture to the ${}^8\text{B}$ halo. The radiative capture process and the astrophysical S-factor was discussed and defined in Chapter 3.1.4.

Radiative capture diagrams

The LO radiative capture diagrams for a P-wave proton-core interaction are shown in Figs. 3.7 and 3.8. All these diagrams consist of an incoming Coulomb wavefunction and a final bound state. While the diagrams in Fig. 3.7 are effectively at tree level, the ones in Fig. 3.8 are more involved due to the photon-leg being attached on the momentum loop. Below we will evaluate these diagrams, with spin quantum numbers appropriate for the reaction ${}^7\text{Be}(p, \gamma){}^8\text{B}$.

Let us start with the diagram in Fig. 3.7(a). The photon-dicluster interaction vertex is proportional to the momentum flowing into the vertex, in Coulomb gauge, and as such this diagram is identically zero in the zero-momentum frame:

$$i\mathcal{A}_{1(\sigma a)}^{i(\alpha)} = 0 \quad (3.53)$$

Note that we have defined the amplitude with a few indices. There is one spin-2 halo-state index α , which will be summed over, and two incoming-particle indices σ , for the spin-1/2 proton field, and a , for the spin-3/2 ground

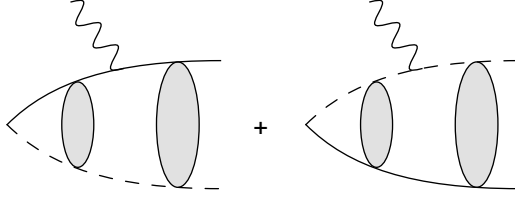


Figure 3.8: Radiative capture diagram, where the incoming proton and core interact with the real vector photon. Since the formed halo bound state is due to a P-wave interaction, the incoming proton-core pair is in a relative S- or D-wave, if only E1 capture is considered.

state core field, which will be averaged over. These matter-field indices are in parentheses. The superscript i will be contracted by the photon polarization vectors. The next two amplitudes below also have these indices.

The next diagram, Fig. 3.7(b), is effectively at tree level. To see this we write it in momentum space, with a loop-integration over the Coulomb wavefunction:

$$\begin{aligned} i\mathcal{A}_{2(\sigma a)}^{i(\alpha)} &= ie(1 - f(Z_c + 1)) (g_1 \mathcal{C}_{ki}^\alpha \mathcal{C}_{\sigma a}^k + g_2 \mathcal{C}_{\beta i}^\alpha \mathcal{C}_{\sigma a}^\beta) \int \frac{d^3k}{(2\pi^3)} \psi_{\mathbf{p}}(\mathbf{k}) \\ &= ie(1 - f(Z_c + 1)) (g_1 \mathcal{C}_{ki}^\alpha \mathcal{C}_{\sigma a}^k + g_2 \mathcal{C}_{\beta i}^\alpha \mathcal{C}_{\sigma a}^\beta) \psi_{\mathbf{p}}(0) \end{aligned} \quad (3.54)$$

In writing down the amplitude (3.54) we have used the Feynman rules for the vector-photon coupling to the contact vertex between the matter particles. These rules are given in Eqs. (3.40) and (3.41). The reason why the integration of the momentum-space Coulomb wavefunction simply gives a coordinate-space Coulomb wavefunction at zero separation can be seen by Fourier transforming the wavefunction and then using the resulting coordinate-space Dirac delta. Note that this contribution is completely from an incoming S-wave, since the incoming Coulomb wavefunction is evaluated at zero separation $\psi_{\mathbf{p}}(0)$.

The third contribution to the capture amplitude is from the loop-diagrams in Fig. 3.8, where the photon leg is attached to either the core or the proton field. The proton and the core propagates down to zero separation after the interaction with the photon, thereby forming a loop. The loop-integral in momentum space is given by

$$\begin{aligned} i\mathcal{A}_{3(\sigma a)}^{i(\alpha)} &= i (g_1 \mathcal{C}_{kj}^\alpha \mathcal{C}_{\sigma a}^k + g_2 \mathcal{C}_{\beta j}^\alpha \mathcal{C}_{\sigma a}^\beta) \\ &\quad \times \int \frac{d^3k_1 d^3k_2}{(2\pi)^6} k_2^j \langle \mathbf{k}_2 | G_C(-B) | \mathbf{k}_1 + f\mathbf{Q} \rangle \left(-i \frac{feZ_c(-k_1^i)}{m_R} \right) \psi_{\mathbf{p}}(\mathbf{k}_1) \\ &\quad - [(f \rightarrow 1 - f), (Z_c \rightarrow 1)] , \end{aligned} \quad (3.55)$$

where the first and second (third) row comes from when the photon is attached to the core (proton) field. In writing down this amplitude we have used the contact interaction Feynman rules (3.37) and (3.38), and the Feynman rules for an A_i photon coupling to the core and proton fields (3.9) and (3.10). The minus sign on the third row can be traced back to the Feynman rules for a vector photon coupling to the core and proton fields, since in the c.m. frame the proton and core momenta are opposite.

Using Eq. (B.29) to replace the Coulomb Green's function with its partial-wave-projected form, and transforming the momentum space kets and bras to coordinate space, we rewrite Eq. (3.55) as

$$\begin{aligned}
i\mathcal{A}_{3(\sigma a)}^{i(\alpha)} &= -i \left(g_1 \mathcal{C}_{kj}^\alpha \mathcal{C}_{\sigma a}^k + g_2 \mathcal{C}_{\beta j}^\alpha \mathcal{C}_{\sigma a}^\beta \right) \frac{3feZ_c}{m_R} \int \frac{d^3k_1}{(2\pi)^3} d^3r_1 d^3r_2 \\
&\quad \times \lim_{r' \rightarrow 0} \left(\frac{G_C^{(1)}(-B; r', r_1)}{r'} \right) \hat{r}_1^j \\
&\quad \times (-i\nabla_2^i) \exp(-i\mathbf{r}_1 \cdot (\mathbf{k}_1 + f\mathbf{Q}) + i\mathbf{r}_2 \cdot \mathbf{k}_1) \psi_{\mathbf{p}}(\mathbf{r}_2) \\
&\quad - [(f \rightarrow 1 - f), (Z_c \rightarrow 1)] \\
&= \left(g_1 \mathcal{C}_{kj}^\alpha \mathcal{C}_{\sigma a}^k + g_2 \mathcal{C}_{\beta j}^\alpha \mathcal{C}_{\sigma a}^\beta \right) \frac{3feZ_c}{m_R} \int d^3r \lim_{r' \rightarrow 0} \left(\frac{G_C^{(1)}(-B; r', r)}{r'} \right) \hat{r}^j \\
&\quad \times \exp(-if\mathbf{r} \cdot \mathbf{Q}) \nabla^i \psi_{\mathbf{p}}(\mathbf{r}) \\
&\quad - [(f \rightarrow 1 - f), (Z_c \rightarrow 1)] . \tag{3.56}
\end{aligned}$$

Here we evaluated the momentum integral as a Dirac delta $\delta(\mathbf{r}_1 - \mathbf{r}_2)$ in the second step, and finally we renamed the integration coordinate to \mathbf{r} .

In Eq. (3.56) we have yet not specified the angular momentum of the incoming wave, but there are some restrictions due to the angular integration $\int d\Omega \hat{r}^j \exp(-if\mathbf{r} \cdot \mathbf{Q}) \nabla^i \psi_{\mathbf{p}}(\mathbf{r})$. However, since we focus our interest here on the threshold properties of the capture process, $|\mathbf{Q}| = \omega \rightarrow 0$, we expand both $\exp(-if\mathbf{r} \cdot \mathbf{Q})$ and $\psi_{\mathbf{p}}(\mathbf{r})$ in Legendre polynomials (or spherical harmonics) and keep only the zeroth order terms, using Eq. (A.2). The derivative then reduces to $\nabla^i \rightarrow \hat{r}^i p \partial_\rho$. The result of the angular integration is therefore

$$\int d\Omega \hat{r}^j \hat{r}^i = \frac{4\pi}{3} \delta^{ij} . \tag{3.57}$$

What we have done is simply to consider only an incoming S-wave and to remove a negligible j_2 spherical Bessel function (we can also replace $j_0 \rightarrow 1$ as it would not change our low-energy results). In order to give a good description of the radiative capture cross section away from threshold, the

incoming D-wave must also be include together with diagrams with initial-wave scattering. Note that we have included the initial Coulomb scattering to all orders, but not scattering due to contact interactions between the matter particles. The procedure for a calculation with incoming D-waves is a straightforward extension of the results that we present here.

Simplifying Eq. (3.56) under the assumptions discussed around Eq. (3.57), and using Eq. (A.28) to replace the limit of the partial-wave projected Coulomb Green's function with a Whittaker function, the resulting loop-integral is

$$\begin{aligned}
i\mathcal{A}_{3(\sigma a)}^{i(\alpha)} = & - \left(g_1 \mathcal{C}_{ki}^\alpha \mathcal{C}_{\sigma a}^k + g_2 \mathcal{C}_{\beta i}^\alpha \mathcal{C}_{\sigma a}^\beta \right) \frac{2\gamma p}{3} \Gamma(2 + k_C/\gamma) \exp(i\sigma_0) \\
& \times \int dr r W_{-k_C/\gamma, 3/2}(2\gamma r) j_0(f\omega r) \partial_\rho \left(\frac{F_0(\eta, \rho)}{\rho} \right) \\
& - [(f \rightarrow 1 - f), (Z_c \rightarrow 1)] , \tag{3.58}
\end{aligned}$$

where $\eta = k_C/p$ and $\rho = pr$ for incoming relative momentum p . This integral is easily evaluated by numerical integration.

The two non-zero contributions, (3.54) and (3.58), depend on the indices α, σ, a and i in the same fashion. Therefore, as the amplitudes are added together and squared, the Clebsch-Gordan coefficients can be treated separately as

$$\frac{1}{2 \times 4} \left(g_1 \mathcal{C}_{ki}^\alpha \mathcal{C}_{\sigma a}^k + g_2 \mathcal{C}_{\beta i}^\alpha \mathcal{C}_{\sigma a}^\beta \right) \left(g_1 \mathcal{C}_{k'i'}^\alpha \mathcal{C}_{\sigma a}^{k'} + g_2 \mathcal{C}_{\beta' i'}^\alpha \mathcal{C}_{\sigma a}^{\beta'} \right)^* = \frac{5}{24} g^2 \delta^{ii'} . \tag{3.59}$$

Here, summation over all the repeated indices is understood. Remember that we have defined $g^2 = g_1^2 + g_2^2$. Thus, using Eq. (B.15) to go from the amplitudes to the cross section, we are ready to give results for the radiative capture cross section and the S-factor $S(E) = E \exp(2\pi\eta)\sigma_{\text{tot}}(E)$.

The S-factor for ${}^7\text{Be}(p, \gamma){}^8\text{B}$

As an example of the P-wave radiative capture formalism above, we present S-factor results for the ${}^7\text{Be}(p, \gamma){}^8\text{B}$ reaction. As input parameters we use the binding momentum γ of the ${}^8\text{B}$ one-proton halo and the ANCs for the $S = 1, 2$ channels A_1 and A_2 . The ANCs were discussed in Chapter 3.2.2 and we use three different sets of ANCs, those by Nollett and Wiringa [35], Navrátil et al. [36] and Tabacaru et al. [37], see Table 3.3. In the subsequent section, we shall instead correlate the threshold S-factor with the charge radius of ${}^8\text{B}$.

The resulting S-factor, using ANCs as input, is shown in black in Fig. 3.9, together with experimental data from Refs. [38, 39, 40, 41, 42, 43, 44, 45].

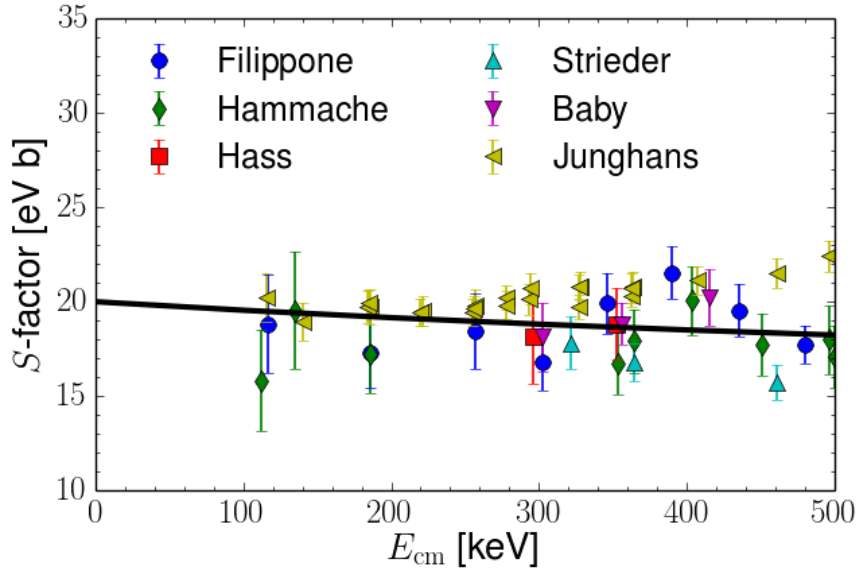


Figure 3.9: The S-factor for the radiative capture reaction ${}^7\text{Be}(p, \gamma){}^8\text{B}$ as a function of c.m. energy. The data are from Refs. [38, 39, 40, 41, 42, 43, 44, 45] and the solid line is the LO Cluster EFT result using the “Nollett” ANCs as input.

The Cluster EFT result presented here follows the experimental data well for low energies, but at higher energies there will be an increasing discrepancy due to the non-inclusion of initial-wave scattering, the M1-resonance plus higher-order operators. In addition, the neglected D-wave component of the incoming Coulomb wavefunction becomes important for higher energies. The obtained threshold value, using the different available ANCs, is

$$S(0) = \begin{cases} (20.0 \pm 1.4) \text{ eV b} & (\text{Nollett ANCs}) \\ 18.9 \text{ eV b} & (\text{Navrátil ANCs}) \\ (17.3 \pm 3.0) \text{ eV b} & (\text{Tabacaru ANCs}) \end{cases} . \quad (3.60)$$

These Cluster EFT results are in accordance with the currently accepted value [18], obtained through extrapolation of compiled experimental data, $S(0) = (20.8 \pm 0.7(\text{expt.}) \pm 1.4(\text{theor.})) \text{ eV b}$. For Cluster EFT results with initial-wave scattering and the D-wave component included, see Zhang et al. [22].

The error presented for the Cluster EFT result (3.60) is due to the error on the input ANCs. However, there is also an EFT error due to the calculation being at LO. We can separate the EFT error into two distinct parts: (i) The error due to the contact interactions being at LO, that is the exclusion of low-

energy scattering parameters in the ERE above the effective range term and (ii) the exclusion of short-range photon-interaction vertices. Since ANCs are used as input, there will be an error on the low-energy scattering parameters extracted, of the order of the EFT expansion parameter. However, due to the fact that the threshold S-factor is directly proportional to the LSZ factor, which in turn is proportional to the ANCs squared, there is no need to extract the effective range parameters to predict the S-factor. This means that there is no EFT error due to the ERE since the ANCs are used as input. The higher-order photon couplings must enter with additional powers of the photon energy ω . Therefore, at threshold, the estimated EFT error due to short-range photon operators is of the order ω/k_{hi} , which is tiny. For one-proton separation energies much smaller than the total mass of the system, the energy of the photon is approximately given by $\omega \approx B$ and therefore, for the ${}^8\text{B}$ system under consideration, the EFT error is $\sim 0.3\%$, using $B = 0.1375$ MeV and $k_{\text{hi}} \sim k_{\alpha} = 50.86$ MeV. We therefore have an almost negligible EFT error at threshold for the S-factor. Note however that the error due to the short-range photon couplings should grow with energy; for example at a c.m. energy $E = 2$ MeV this error should be of order $\sim 4\%$. In addition, at these energies there are also errors due to the neglected D-wave component and initial-wave scattering [22].

While the result of this section is interesting on its own, the main result of our work on the ${}^7\text{Be}(p, \gamma){}^8\text{B}$ reaction is when this reaction is put in relation to the charge radius of the halo nucleus ${}^8\text{B}$. We will now turn our attention to the correlation of these two observables.

3.2.5 Correlating the threshold S-factor and charge radius of ${}^8\text{B}$

In this section we use the fact that both the threshold S-factor for the radiative capture reaction ${}^7\text{Be}(p, \gamma){}^8\text{B}$ and the charge radius of ${}^8\text{B}$ are free of short-range operators at LO. This will allow us to show a LO correlation between these two observables. Such a correlation is very useful since it is experimentally very difficult to measure the low-energy capture cross section, while a very precise charge radius measurement of ${}^8\text{B}$ is planned to take place in the near future. The charge radius will be measured through the atomic isotope shift, which should be very accurate. However, the resulting charge radius is then given relative to that of another boron isotope. The main source of error in such a measurement is therefore expected to be due to the uncertainty in the charge radius of the reference nucleus.

This correlation can be seen as using the effective range, or the sum of

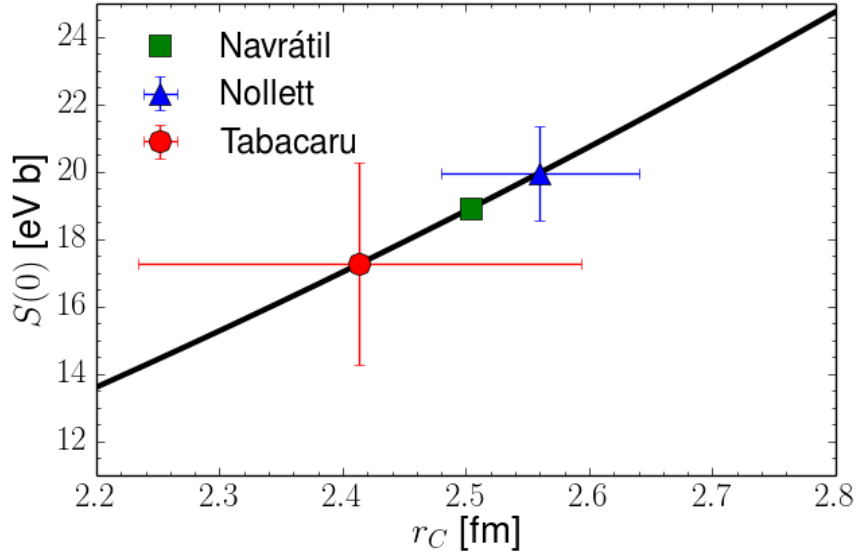


Figure 3.10: The LO Cluster EFT correlation plot, between the threshold S-factor and the charge radius of ${}^8\text{B}$. The three data points with error bars correspond to results obtained with input ANCs from Nollett and Wiringa [35], Navrátil et al. [36] and Tabacaru et al. [37]. The error bars are due to the errors on the extracted ANCs.

squared ground-state ANCs $A_1^2 + A_2^2$, as a free parameter. The parameters k_C , γ , γ_* in Table 3.2 and the excited state ANC, A_* , given in Table 3.3 are used as fixed input for the calculation. Since the correlation is at LO, the expected EFT error for the charge radius is 29%, as discussed above in Chapter 3.2.2. This uncertainty is too large to be able to compete with more sophisticated methods. However, if the EFT for this system can be extended to include more physics or if an actual higher-order calculation can be made, the error can be brought down. At that point this procedure would provide a model independent way of determining the threshold S-factor without having to rely on extrapolations.

The LO correlation plot is shown in Fig. 3.10. The solid line shows the Cluster EFT correlation result, while the triangle, square and circle show the Cluster EFT results using the ANCs from Nollett, Navrátil and Tabacaru, respectively. For this LO Cluster EFT prediction, only points on the solid line are allowed, and these points correspond to different values of the effective range, or the sum of squared ground-state ANCs $A_1^2 + A_2^2$. The error bars shown in the correlation plot are due to the errors on the extracted ANCs. The expected EFT error of 29% on the charge radius squared is understood

to be present. Note that due to this large EFT error a measurement of the ${}^8\text{B}$ charge radius of around 2.8 fm would be consistent with a threshold S-factor of 20 eV b, as can be seen by comparing the charge radius result with EFT errors (3.52) and the correlation plot Fig. 3.10.

Chapter 4

Discussion and outlook

In this thesis we have introduced Cluster EFT formalism for one-proton halo nuclei, bound in a relative S- or P-wave. This formalism was applied to study the halo states $^{17}\text{F}^*$ and ^8B . The main results presented were the calculations of the charge radii and radiative capture S-factors for these states, and the LO correlation between these two observables.

For the S-wave one-proton halos, we presented NLO results with the effective-range correction included. However, due to the fine-tuning of the $^{17}\text{F}^*$ system, we argued that the effective range correction should be included already at LO. This fine-tuning also makes it more difficult to proceed to higher order, since it promotes certain short-range operators. For example, there is an operator for the charge radius at the next order, that we only can fix to this observable as of now. Given that this short-range parameter can indeed not be fitted to anything but the charge radius, then the two-body Cluster EFT treatment of the charge radius of $^{17}\text{F}^*$ is restricted to LO only. For the radiative capture cross section, there also exist short-range operators, which enter with an additional dependence on the photon energy. However, since the astrophysical interest is mainly in the extreme low-energy regime of the process, the high-energy physics is not of key importance.

When it comes to the P-wave interaction, the effective range is needed at LO by renormalization. This complicates the question of predictive power, since two parameters are needed already at LO. In this thesis we have been able to fix this extra parameter by using either the derived correlation with the charge radius, or by employing extracted ANCs as input. We applied the formalism to study the ^8B halo nucleus. A main result was the LO correlation between the threshold S-factor and the charge radius. Results were also presented using the ANCs as input and the S-factor result was in good agreement with data and the accepted value at threshold. However, the presented Cluster EFT result will be accompanied by larger uncertainties

at higher energies, due to the non-inclusion of initial-wave scattering, the neglected D-wave component of the incoming wavefunction, and the presence of the M1-resonance. Also, at higher energies the short-range operators from higher orders will contribute. The charge radius prediction is most likely too small, but the result comes with a large EFT error. In addition, for the P-wave system considered, there is a short-range operator at the next order for the charge radius. Thus, it seems as though the charge radius is restricted to a LO treatment only.

A natural extension of the work presented in this thesis is to consider three-body systems as well. In the context of charged three-body systems the Hoyle state in ^{12}C is of course of interest, but also the two-proton halo nucleus ^{17}Ne . Furthermore, as discussed in this thesis, there are short-range operators present at low order for the observable charge radius, and these limit the predictive power of the Cluster EFT. It would therefore be interesting to treat these same systems in a three-body formalism, for example ^8B as consisting of an α -particle, a ^3He and a proton. Such an extension would then serve as a way to circumvent the present limitations. However, to describe such systems in a Cluster EFT formalism one would need to derive three-body Coulomb propagators and, for that reason, a more straightforward outlook would be to consider three-body systems with only two charged particles, for example the ^8Li nucleus treated as consisting of an α -particle, a triton and a neutron. The first step in this direction, however, would be to consider three-body systems without Coulomb interactions. The two-neutron halo nucleus ^{26}O is an interesting example, but would require the treatment of resonant D-wave interactions.

A final outlook, that is relatively straightforward, is to simply consider more states or systems using this same formalism. For example, to include the ground state of ^{17}F as an explicit degree-of-freedom into the $^{16}\text{O}+\text{proton}$ field theory. This state is bound due to a D-wave interaction, which of course increases the complexity, but the hope is that this ground state is less fine-tuned than the excited state. When including this state, a more complete picture of the radiative capture cross section can be given at finite energies. Other systems to consider would be ^7Be and ^7Li , as an α -particle and a ^3He or a triton, respectively.

Appendix A

Coulomb effects in effective field theory

For low momenta the Coulomb interaction must be included to all orders and we do this by using the full Coulomb propagator G_C , shown in Fig. A.1. The Coulomb propagator, or Coulomb Green's function, can be written in the spectral representation as

$$\langle \mathbf{r} | G_C(E) | \mathbf{r}' \rangle = \int \frac{d^3p}{(2\pi)^3} \frac{\psi_{\mathbf{p}}(\mathbf{r}) \psi_{\mathbf{p}}^*(\mathbf{r}')}{E - \mathbf{p}^2/(2m_R) + i\varepsilon}, \quad (\text{A.1})$$

where we have represented it in coordinate space. We define the Coulomb wavefunction $\psi_{\mathbf{p}}(\mathbf{r})$ by its partial wave expansion

$$\psi_{\mathbf{p}}(\mathbf{r}) = \sum_{l=0}^{\infty} (2l+1) i^l \exp(i\sigma_l) \frac{F_l(\eta, \rho)}{\rho} P_l(\hat{\mathbf{p}} \cdot \hat{\mathbf{r}}). \quad (\text{A.2})$$

Here we have defined $\rho = pr$ and $\eta = k_C/p$, with the Coulomb momentum $k_C = Z_1 Z_2 \alpha m_R$, where Z_1 and Z_2 are the proton number of the clusters and α is the fine structure constant. We also define the pure Coulomb phase shift $\sigma_l = \arg \Gamma(l+1+i\eta)$. The partial-wave projected Coulomb wavefunctions F_l and G_l can be expressed in terms of the Whittaker functions. The regular wavefunction F_l is written using the Whittaker M-function according to

$$F_l(\eta, \rho) = A_l(\eta) M_{i\eta, l+1/2}(2i\rho), \quad (\text{A.3})$$

with A_l defined as

$$A_l(\eta) = \frac{|\Gamma(l+1+i\eta)| \exp[-\pi\eta/2 - i(l+1)\pi/2]}{2(2l+1)!}. \quad (\text{A.4})$$

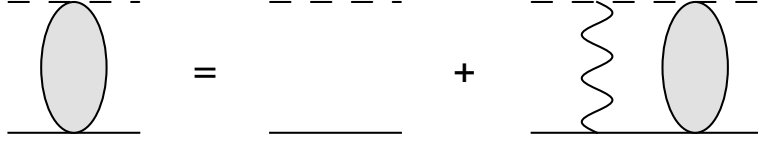


Figure A.1: The Coulomb propagator, defined recursively. The shaded blob denotes the resummation of the Coulomb interaction.

The irregular Coulomb wave function, G_l , is given by

$$G_l(\eta, \rho) = iF_l(\eta, \rho) + B_l(\eta)W_{i\eta, l+1/2}(2i\rho) , \quad (\text{A.5})$$

where W is the Whittaker W -function and the coefficient B_l is defined as

$$B_l(\eta) = \frac{\exp(\pi\eta/2 + i\pi/2)}{\arg \Gamma(l+1+i\eta)} . \quad (\text{A.6})$$

Since we work with both-bound state and free Coulomb wavefunctions it is important to note that the absolute value and the argument of the Gamma-function are defined as

$$|\Gamma(l+1+i\eta)| = \sqrt{\Gamma(l+1+i\eta)\Gamma(l+1-i\eta)} \quad (\text{A.7})$$

and

$$\arg \Gamma(l+1+i\eta) = \sqrt{\frac{\Gamma(l+1+i\eta)}{\Gamma(l+1-i\eta)}} . \quad (\text{A.8})$$

The Gamow-Sommerfeld factor $C_\eta^2 = |\psi(0)|^2$ is given by

$$C_\eta^2 = C(0, \eta)^2 = \frac{2\pi\eta}{\exp(2\pi\eta) - 1} \quad (\text{A.9})$$

$$= \exp(-\pi\eta)\Gamma(1+i\eta)\Gamma(1-i\eta) \quad (\text{A.10})$$

and we will also need its generalization to higher partial waves

$$C(l, \eta)^2 = \exp(-\pi\eta)\Gamma(l+1+i\eta)\Gamma(l+1-i\eta) . \quad (\text{A.11})$$

Note in particular that

$$C(1, \eta)^2 = (1 + \eta^2)C_\eta^2 . \quad (\text{A.12})$$

The total phase shift we write as $\sigma_l + \delta_l$ and the Coulomb-modified phase shift δ_l is what we refer to as the phase shift. The Coulomb-modified ERE defines

the Coulomb-modified low-energy scattering parameters a_l, r_l, \dots through the phase shift:

$$k^{2l+1}C(l, \eta)^2(\cot \delta_l - i) + 2k_C h_l(\eta) = -\frac{1}{a_l} + \frac{1}{2}r_l k^2 + \dots \quad (\text{A.13})$$

The function h_l is given by

$$h_l(\eta) = p^{2l} \frac{C(l, \eta)^2}{C(0, \eta)^2} \left(\psi(i\eta) + \frac{1}{2i\eta} - \log(i\eta) \right), \quad (\text{A.14})$$

where ψ is the polygamma function.

A.1 Partial-wave projected Coulomb Green's function

We now continue by analyzing the Coulomb Green's function $(\mathbf{r}_1|G_C|\mathbf{r}_2)$. It is useful to express the Green's function in its partial-wave expanded form

$$(\mathbf{r}_1|G_C(E)|\mathbf{r}_2) = \sum_{l=0}^{\infty} (2l+1)G_C^{(l)}(E; r_1, r_2)P_l(\hat{\mathbf{r}}_1 \cdot \hat{\mathbf{r}}_2). \quad (\text{A.15})$$

The form of $G_C^{(l)}$ is derived by expanding the Coulomb wavefunctions in Eq. (A.1), using spherical harmonics

$$\psi_{\mathbf{p}}(\mathbf{r}) = \sum_{l,m} 4\pi i^l \exp(i\sigma_l) \frac{F_l(\eta, \rho)}{\rho} Y_{lm}^*(\theta, \phi) Y_{lm}(\theta, \phi). \quad (\text{A.16})$$

In the first step we use the orthogonality of the harmonics and in the second step the addition theorem is used:

$$\begin{aligned} (\mathbf{r}_1|G_C(E)|\mathbf{r}_2) &= \sum_{l_1 m_1} \sum_{l_2 m_2} \int \frac{d^3 p}{(2\pi)^3} (4\pi)^2 \frac{i^{l_1-l_2} \exp(i\sigma_{l_1} - i\sigma_{l_2}) \frac{F_{l_1}(\eta, \rho_1)}{\rho_1} \frac{F_{l_2}^*(\eta, \rho_2)}{\rho_2}}{E - \frac{\mathbf{p}^2}{2m_R}} \\ &\quad \times Y_{l_1 m_1}(\theta_1, \varphi_1) Y_{l_1 m_1}^*(\theta_p, \varphi_p) Y_{l_2 m_2}(\theta_p, \varphi_p) Y_{l_2 m_2}^*(\theta_2, \varphi_2) \\ &= \sum_{lm} \int \frac{d^3 p}{(2\pi)^3} 4\pi \frac{F_l(\eta, \rho_1) F_l^*(\eta, \rho_2)}{\rho_1 \rho_2} \frac{1}{E - \frac{\mathbf{p}^2}{2m_R}} \\ &\quad \times Y_{lm}(\theta_1, \varphi_1) Y_{lm}^*(\theta_2, \varphi_2) \\ &= \sum_l (2l+1) P_l(\hat{\mathbf{r}}_1 \cdot \hat{\mathbf{r}}_2) \int \frac{d^3 p}{(2\pi)^3} \frac{F_l(\eta, \rho_1) F_l^*(\eta, \rho_2)}{\rho_1 \rho_2} \frac{1}{E - \frac{\mathbf{p}^2}{2m_R}} \end{aligned} \quad (\text{A.17})$$

Thus, comparing Eqs. (A.15) and (A.17), the Green's function for a specific partial wave is given by

$$G_C^{(l)}(E; r_1, r_2) = \int \frac{d^3p}{(2\pi)^3} \frac{F_l(\eta, \rho_1) F_l^*(\eta, \rho_2)}{\rho_1 \rho_2} \frac{1}{E - \frac{\mathbf{p}^2}{2m_R}}. \quad (\text{A.18})$$

It is convenient to use the Coulomb Green's function in a non-integral form and below we present such a form for the bound-state Green's function. This can be done by doing a partial-wave projection and forming the Green's function as a product between two independent Coulomb wavefunctions, satisfying one boundary condition each, in accordance with the definition of Green's function. For the $r = 0$ boundary condition we must use the regular Coulomb wave function F_l and to satisfy the condition for a bound state at $r = \infty$ we need to form the combination

$$iF_l + G_l. \quad (\text{A.19})$$

This can be seen from the $r \rightarrow \infty$ asymptotics

$$F_l(\eta, \rho) \rightarrow \sin(\rho - l\pi/2 - \eta \log(2\rho) + \sigma_l) \quad (\text{A.20})$$

and

$$G_l(\eta, \rho) \rightarrow \cos(\rho - l\pi/2 - \eta \log(2\rho) + \sigma_l), \quad (\text{A.21})$$

using that for a bound state $\rho = i\gamma r$, with $\gamma > 0$, where the only combination that yields only an $\exp(-\gamma r)$ dependence is the combination given in (A.19). Therefore, the partial-wave projected Coulomb Green's function is

$$G_C^{(l)}(-B; \rho', \rho) = -\frac{m_R p}{2\pi} \frac{F_l(\eta, \rho') [iF_l(\eta, \rho) + G_l(\eta, \rho)]}{\rho' \rho}. \quad (\text{A.22})$$

The normalization is given by the discontinuity of the slope at $\rho = \rho'$, according to

$$(\partial_{r'} - \partial_r) G_C(E; pr', pr) \Big|_{\rho' \rightarrow \rho} = \frac{1}{f(r)}, \quad (\text{A.23})$$

where $f(r) = 2\pi r^2/m_R$ for the Schrödinger-Coulomb equation.

Many of the diagrams we consider will have a factor of a Coulomb Green's function with one end at zero separation. Using the identity

$$iF_l(\eta, \rho) + G_l(\eta, \rho) = \exp(i\sigma_l + \pi\eta/2 - li\pi/2) W_{-i\eta, l+1/2}(-2i\rho) \quad (\text{A.24})$$

and the limits

$$\lim_{\rho \rightarrow 0} \frac{F_0(\eta, \rho)}{\rho} = \exp(-\pi\eta/2) \sqrt{\Gamma(1+i\eta)\Gamma(1-i\eta)} \quad (\text{A.25})$$

$$\lim_{r \rightarrow 0} \left(\frac{F_1(\eta, \rho)}{\rho^2} \right) = \frac{1}{3} \exp(-\pi\eta/2) \sqrt{\Gamma(2+i\eta)\Gamma(2-i\eta)} \quad (\text{A.26})$$

we can write the relevant objects for propagation down to zero separation as

$$G_C^{(0)}(-B; 0, \rho) = -\frac{m_{\text{RP}}}{2\pi} \Gamma(1+i\eta) \frac{W_{-i\eta, 1/2}(-2i\rho)}{\rho} \quad (\text{A.27})$$

for S-wave interactions and

$$\lim_{\rho' \rightarrow 0} \left(\frac{G_C^{(1)}(E; r', r)}{\rho'} \right) = i \frac{m_{\text{RP}}}{6\pi} \Gamma(2+i\eta) \frac{W_{-i\eta, 3/2}(-2i\rho)}{\rho} \quad (\text{A.28})$$

for P-wave interactions. These results, Eqs. (A.27) and (A.28), we use when we solve the loop-integrals in Chapter 3 numerically.

Appendix B

Proton halo diagrams

B.1 Elastic scattering and bound state properties for an S-wave interaction

Using the full dicluster propagator Eq. (3.13) we write the S-wave elastic scattering t-matrix as

$$iT_0(E) = ig^2 \exp(2i\sigma_0) C_\eta^2 D(E, 0) . \quad (\text{B.1})$$

The t-matrix can be written in terms of the Coulomb-strong phase shift δ_0 , according to [17]

$$T_0(E) = -\frac{2\pi}{m_{\text{R}}} \frac{\exp(2i\sigma_0)}{k(\cot \delta_0 - i)} . \quad (\text{B.2})$$

The S-wave Coulomb-modified ERE is given in Eq. (A.13), which for an S-wave interaction is

$$kC_\eta^2(\cot \delta_0 - i) + 2k_C h_0(\eta) = -\frac{1}{a_0} + \frac{1}{2}r_0 k^2 + \dots , \quad (\text{B.3})$$

where a_0 and r_0 are the Coulomb-modified scattering length and effective range, respectively. One should note that the imaginary part of $2k_C h_0(\eta)$ exactly cancels $-ikC_\eta^2$. Combining Eqs. (3.13), (B.1) and (B.2) together with the Coulomb-modified ERE Eq. (B.3), we arrive at the renormalization conditions

$$\frac{1}{a_0} = \frac{2\pi}{g^2 m_{\text{R}}} (\Delta + \Sigma^{\text{div}}) \quad (\text{B.4})$$

$$r_0 = -\frac{2\pi\nu}{g^2 m_{\text{R}}^2} \quad (\text{B.5})$$

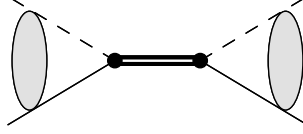


Figure B.1: The elastic scattering diagram for a proton-core pair scattering to all orders in the strong interaction, using the full halo propagator as the intermediate field. Note that the Coulomb interaction is also taken to infinite order.

for the EFT parameters g and Δ , in the Lagrangian (3.1). Note that only one renormalization $\Delta_{\text{Ren}} = \Delta + \Sigma^{\text{div}}$ is needed for the S-wave interaction.

From the full dicluster propagator we can write down the wavefunction renormalization, or LSZ residue,

$$\begin{aligned} \mathcal{Z} &= \left[\frac{d(D(E)^{-1})}{dE} \right]^{-1} \Big|_{E=-B} \\ &= \frac{1}{\nu + \Sigma'(E)} \Big|_{E=-B} . \end{aligned} \quad (\text{B.6})$$

Using Eqs. (3.15) and (B.5) the wavefunction renormalization can be written in terms of the effective range as

$$\mathcal{Z} = \frac{6\pi k_C}{g^2 m_R^2} \left[-3k_C r_0 + \frac{6k_C^2}{m_R} \frac{d}{dE} h_0(\eta) \right]^{-1} \Big|_{E=-B} . \quad (\text{B.7})$$

If the effective range is treated as a NLO correction, then the LO wavefunction renormalization is given by

$$\mathcal{Z} = \frac{6\pi k_C}{g^2 m_R^2} \left[\frac{6k_C^2}{m_R} \frac{d}{dE} h_0(\eta) \right]^{-1} \Big|_{E=-B} . \quad (\text{B.8})$$

One should note that the for small γ_0/k_C the expansion

$$\frac{6k_C^2}{m_R} \frac{d}{dE} H(\eta) = 1 - \frac{\gamma^2}{5k_C^2} + \frac{\gamma^4}{7k_C^4} + \dots \quad (\text{B.9})$$

can be used to simplify Eqs. (B.7) and (B.8), that is if we write the LSZ residue Eq. (B.7) using Eq. (B.9) we get

$$\mathcal{Z} = \frac{6\pi k_C}{g^2 m_R^2} \frac{1}{1 - 3k_C r_0} + \mathcal{O}\left(\frac{\gamma^2}{k_C^2}\right) . \quad (\text{B.10})$$

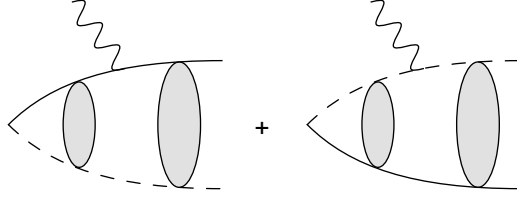


Figure B.2: Radiative capture diagram, where the incoming proton and core each interact with the real vector photon. Since the formed halo bound state is due to an S-wave interaction the incoming proton-core pair is in a relative P-wave, if only E1 capture is considered.

B.2 Radiative capture diagrams for an S-wave interaction

In Fig. B.2 the radiative capture diagram to NLO is shown. It consists of an incoming Coulomb wavefunction, the proton-photon or core-photon interaction and the propagation down to the bound state, at zero separation, with a Coulomb propagator.

We first write this loop-diagram in momentum space, with \mathbf{p} being the relative momentum of the incoming proton-core pair and \mathbf{k} the momentum of the outgoing photon:

$$i\mathcal{A}_{\text{loop}} = g\sqrt{Z} \frac{eZ_c f}{m_R} \int \frac{d^3k_2 d^3k_1}{(2\pi)^6} \langle \mathbf{k}_2 | G_C(-B) | \mathbf{k}_1 + f\mathbf{k} \rangle \mathbf{k}_1 \psi_{\mathbf{p}}(\mathbf{k}_1) - [(f \rightarrow 1-f), (Z_c \rightarrow 1)] \quad (\text{B.11})$$

Fourier transforming both sides of the Coulomb propagator and the Coulomb wavefunction, we can replace the remaining \mathbf{k}_1 with a $-i\nabla$ acting on a Dirac delta. The resulting coordinate space integral is then given by

$$i\mathcal{A}_{\text{loop}} = g\sqrt{Z} \frac{eZ_c f}{m_R} \int d^3r G_C^{(0)}(-B; 0, \rho) \exp(-if\mathbf{k} \cdot \mathbf{r}) \nabla \psi_{\mathbf{p}}(\mathbf{r}) - [(f \rightarrow 1-f), (Z_c \rightarrow 1)] \quad (\text{B.12})$$

Note that the amplitude Eq. (B.12) is a vector quantity, due to the ∇ , and that it will be multiplied by the photon polarization vectors. From current conservation we have the Ward identity

$$\epsilon_i \cdot \mathbf{k} = 0 \quad (\text{B.13})$$

and thus, choosing the photon momentum along the z-axis $\mathbf{k} = \omega \hat{z}$, we can choose as photon polarization vectors $\epsilon_1 = \hat{x}$ and $\epsilon_2 = \hat{y}$.

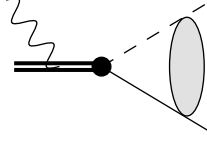


Figure B.3: Tree-level diagram for the radiative capture process, which evaluates to zero in the zero-momentum frame.

If the resulting halo state is a $1/2^+$ and the core is a 0^+ , such as the $^{17}\text{F}^*$ system with an ^{16}O core, then the E1 capture channel will be through an initial P-wave. We can see this from Eq. (B.12), since by keeping only the first term in the expansion $\exp(-i\mathbf{k}\cdot\mathbf{r}) = \sum_l 2i^l j_l(fkr) P_l(\hat{k}\cdot\hat{r})$ the angular integration picks out only the P-wave in the Coulomb wavefunction Eq. (A.2). Thus, the squared amplitude multiplied with the photon polarization vectors becomes

$$\begin{aligned} \sum_i |\epsilon_i \cdot \mathcal{A}|^2 &= \left| \sqrt{Z} \sin\theta (\cos\phi + \sin\phi) \frac{4\pi g e Z_c f \exp(i\sigma_1)}{m_{\text{R}} p} \right. \\ &\quad \times \int dr G_{\text{C}}^{(0)}(-B; 0, \rho) j_0(f\omega r) \frac{\partial}{\partial r} [r F_1(k_{\text{C}}/p, pr)] \\ &\quad \left. - [(f \rightarrow 1-f), (Z_c \rightarrow 1)] \right|^2. \end{aligned} \quad (\text{B.14})$$

The differential cross section is evaluated in terms of the amplitude as

$$\frac{d\sigma}{d\Omega} = \frac{m_{\text{R}}\omega}{8\pi^2 p} \sum_i |\epsilon_i \cdot \mathcal{A}|^2 \quad (\text{B.15})$$

and the total cross section is obtained by integration over the solid angle $d\Omega$.

We also have a tree-level diagram $\mathcal{A}_{\text{tree}}$, as shown in Fig. B.3, which comes in with the Feynman rule for the interaction between the vector photon and the dicluster field. Since this interaction is proportional to the momentum flowing along the dicluster into the vertex, in Coulomb gauge, this amplitude is zero in the zero-momentum frame.

B.3 P-wave interactions

The most basic object in the loop-integrals is the $\mathbf{X}_1(E_{\mathbf{p}})$ vector integral, defined as

$$\mathbf{X}_1(E_{\mathbf{p}}) = \int \frac{d^3k}{(2\pi)^3} \mathbf{k} \psi_{\mathbf{p}}(\mathbf{k}). \quad (\text{B.16})$$

We evaluate the integral Eq. (B.16) by Fourier transforming the Coulomb wavefunction ψ and then letting the $\mathbf{k} \mapsto -i\nabla$, as it acts on a plane wave:

$$\begin{aligned}
\mathbf{X}_1(E_{\mathbf{p}}) &= \int \frac{d^3k}{(2\pi)^3} \mathbf{k} \psi_{\mathbf{p}}(\mathbf{k}) \\
&= \int d^3r \frac{d^3k}{(2\pi)^3} \mathbf{k} \exp(i\mathbf{k} \cdot \mathbf{r}) \psi_{\mathbf{p}}(\mathbf{r}) \\
&= \int d^3r \psi_{\mathbf{p}}(\mathbf{r}) (-i\nabla) \underbrace{\int \frac{d^3k}{(2\pi)^3} \exp(i\mathbf{k} \cdot \mathbf{r})}_{\delta^{(3)}(\mathbf{r})} \\
&= i \int d^3r \delta^{(3)}(\mathbf{r}) (\nabla \psi_{\mathbf{p}}(\mathbf{r}))
\end{aligned} \tag{B.17}$$

The last step is given by the properties of the Dirac delta distribution. Now, the partial wave expansion of the Coulomb wavefunction Eq. (A.2) allow us to write

$$\begin{aligned}
\nabla \psi_{\mathbf{p}}(\mathbf{r}) &= \sum_{l=0}^{\infty} (2l+1) i^l \exp(i\sigma_l) \\
&\quad \times \left[\hat{r} p \partial_{\rho} \frac{F_l(\eta, \rho)}{\rho} P_l(\cos \theta) + \hat{\theta} \frac{p F_l(\eta, \rho)}{\rho^2} \partial_{\theta} P_l(\cos \theta) \right].
\end{aligned} \tag{B.18}$$

Note that for $l = 0$ we get

$$\nabla \psi_{\mathbf{p}}(\mathbf{r}) \Big|_{l=0} = \hat{r} 3i \exp(i\sigma_1) p \partial_{\rho} \frac{F_0(\eta, \rho)}{\rho}, \tag{B.19}$$

which is an odd function of \mathbf{r} . This means that the integration in Eq. (B.17) of the $l = 0$ term is zero. Furthermore, we have that

$$\lim_{\rho \rightarrow 0} \partial_{\rho} \frac{F_l(\eta, \rho)}{\rho} = 0, \quad l > 1 \tag{B.20}$$

and

$$\lim_{\rho \rightarrow 0} \frac{F_l(\eta, \rho)}{\rho^2} = 0, \quad l > 1, \tag{B.21}$$

which means that only the $l = 1$ term will contribute to \mathbf{X}_1 . Summarizing, we then have

$$\begin{aligned}\mathbf{X}_1(E_{\mathbf{p}}) &= \int \frac{d^3k}{(2\pi)^3} \mathbf{k} \psi_{\mathbf{p}}(\mathbf{k}) \\ &= i \times 3i \exp(i\sigma_1) \lim_{\rho \rightarrow 0} \left(\cos(\theta) \hat{r} p \partial_{\rho} \frac{F_1(\eta, \rho)}{\rho} - \sin(\theta) \hat{\theta} p \frac{F_1(\eta, \rho)}{\rho^2} \right) \\ &= -3 \exp(i\sigma_1) \mathbf{p} \lim_{\rho \rightarrow 0} \left(\frac{F_1(\eta, \rho)}{\rho^2} \right) \quad (\text{B.22})\end{aligned}$$

$$= -\exp(i\sigma_1) \mathbf{p} C(1, \eta) . \quad (\text{B.23})$$

In the last steps we used that

$$\cos(\theta) \hat{r} - \sin(\theta) \hat{\theta} = \hat{z} \quad (\text{B.24})$$

and that the limits of $\partial_{\rho}(F_1(\eta, \rho)/\rho)$ and $F_1(\eta, \rho)/\rho^2$ can both be written as

$$\lim_{\rho \rightarrow 0} \left(\partial_{\rho} \frac{F_1(\eta, \rho)}{\rho} \right) = \lim_{\rho \rightarrow 0} \left(\frac{F_1(\eta, \rho)}{\rho^2} \right) = \frac{1}{3} C(1, \eta) . \quad (\text{B.25})$$

Now that we have a closed expression for the \mathbf{X}_1 , we are in a position to simplify the integral

$$I_1(0, \mathbf{r}) = \int \frac{d^3k}{(2\pi)^3} \mathbf{k} \langle \mathbf{k} | G_C(E) | \mathbf{r} \rangle , \quad (\text{B.26})$$

which is present in all loop-diagrams involving a propagation down to a bound P-wave state. Note that the object in Eq. (B.26) is defined with one momentum- and one coordinate-space side, but comparing to the S-wave interaction equivalent

$$\begin{aligned}I_0(0, \mathbf{r}) &= \int \frac{d^3k}{(2\pi)^3} \langle \mathbf{k} | G_C(E) | \mathbf{r} \rangle \\ &= \langle 0 | G_C(E) | \mathbf{r} \rangle \quad (\text{B.27})\end{aligned}$$

we expect that I_1 behaves as if it is a coordinate-space object. We have that, using the spectral representation of the Coulomb Green's function, Eq. (B.22) and doing a partial wave expansion of $\psi_{\mathbf{p}}^*(\mathbf{r})$,

$$\begin{aligned}I_1(0, \mathbf{r}) &= \int \frac{d^3k d^3p}{(2\pi)^6} \mathbf{k} \psi_{\mathbf{p}}(\mathbf{k}) \frac{\psi_{\mathbf{p}}^*(\mathbf{r})}{E - \frac{\mathbf{p}^2}{2m_R}} \\ &= 9i \int \frac{p^2 dp}{(2\pi)^3} \lim_{\rho' \rightarrow 0} \left(\frac{F_1(\eta, \rho')}{\rho'^2} \right) \frac{F_1^*(\eta, \rho)}{\rho} \int d\Omega_{\mathbf{p}} \cos \theta \\ &= 3i \hat{\mathbf{r}} \lim_{r' \rightarrow 0} \left[\frac{1}{r'} \int \frac{d^3p}{(2\pi)^3} \frac{F_1(\eta, \rho')}{\rho'} \frac{F_1^*(\eta, \rho)}{\rho} \frac{1}{E - \frac{\mathbf{p}^2}{2m_R}} \right] . \quad (\text{B.28})\end{aligned}$$

Using Eq. (A.18) we find that

$$\begin{aligned}
I_1(0, \mathbf{r}) &= \int \frac{d^3k}{(2\pi)^3} \mathbf{k} \langle \mathbf{k} | G_C(E) | \mathbf{r} \rangle \\
&= 3i\hat{\mathbf{r}} \lim_{r' \rightarrow 0} \left(\frac{G_C^{(1)}(E; r', r)}{r'} \right). \tag{B.29}
\end{aligned}$$

We like this form since the partial-wave projected Green's function can be written in a closed functional form.

B.3.1 Elastic scattering and bound state properties

The irreducible self-energy $\Sigma_{\alpha\alpha'}$ for the spin-2 dicluster state, with incoming spin α and outgoing spin α' , is of course diagonal and therefore we define

$$\Sigma = \frac{\delta_{\alpha\alpha'}}{5} \Sigma_{\alpha\alpha'}. \tag{B.30}$$

Since the spin indices α and α' come from the products of Clebsch-Gordan coefficients $\mathcal{C}_{ij}^\alpha \mathcal{C}_{a\sigma}^j \mathcal{C}_{i'j'}^\alpha \mathcal{C}_{a\sigma}^{j'} = \delta_{ii'}/3$, $\mathcal{C}_{i\beta}^\alpha \mathcal{C}_{a\sigma}^\beta \mathcal{C}_{i'\beta'}^\alpha \mathcal{C}_{a\sigma}^{\beta'} = \delta_{ii'}/3$ and $\mathcal{C}_{ij}^\alpha \mathcal{C}_{\chi\sigma}^j \mathcal{C}_{i'j'}^\alpha \mathcal{C}_{\chi\sigma}^{j'} = \delta_{ii'}/3$, due to the $S = 1, 2$ channels for the ground state core field and the $S = 1$ channel for the excited state core field, we have that the irreducible self-energy is conveniently written as

$$\Sigma = \frac{\delta_{ii'}}{3} \Sigma_{ii'}. \tag{B.31}$$

Here, the spin indices in $\Sigma_{ii'}$ is simply from the vertex momenta, that is $k_i k_{i'}$, and these momenta are loop-momenta in the irreducible self-energy. The result of this discussion is that the interaction vertices can be replaced by simple factors of $g^2 \mathbf{k} \cdot \mathbf{k}'/3$ and $g_*^2 \mathbf{k} \cdot \mathbf{k}'/3$, for the ground state core field and the excited state core field, respectively.

The momentum-space integral for the irreducible self-energy is, using only the ground-state core field,

$$\begin{aligned}
i\Sigma(E) &= i \frac{g^2}{3} \int \frac{d^3k_1 d^3k_2}{(2\pi)^6} \mathbf{k}_2 \cdot \mathbf{k}_1 \langle \mathbf{k}_2 | G_C(E) | \mathbf{k}_1 \rangle \\
&= i \frac{g^2}{3} \int \frac{d^3p}{(2\pi)^3} \frac{\mathbf{X}_1(E_{\mathbf{p}}) \cdot \mathbf{X}_1^*(E_{\mathbf{p}})}{E - \frac{\mathbf{p}^2}{2m_R}}. \tag{B.32}
\end{aligned}$$

Then using equation (B.23) we have the integral, writing $k^2 = 2m_{\text{R}}E$,

$$\begin{aligned}
i\Sigma(E) &= -i\frac{g^2 m_{\text{R}}}{3\pi^2} \int dp \frac{C(1, \eta)^2 p^4}{p^2 - k^2} \\
&= -i\frac{g^2 m_{\text{R}}}{3\pi^2} \int dp C_{\eta}^2 \left[p^2 + k^2 + k_{\text{C}}^2 + \frac{k_{\text{C}}^2 k^2 + k^4}{p^2 - k^2} \right] \\
&= -ig^2 \left[L_3 + (k_{\text{C}}^2 + k^2)L_1 + (k_{\text{C}}^2 k^2 + k^4)J^{\text{fin}}(k) \right], \tag{B.33}
\end{aligned}$$

where we have defined

$$L_n = \frac{m_{\text{R}}}{3\pi^2} \int dp C_{\eta}^2 p^{n-1} \tag{B.34}$$

and

$$J^{\text{fin}}(k) = \frac{m_{\text{R}}}{3\pi^2} \int dp \frac{C_{\eta}^2}{p^2 - k^2}. \tag{B.35}$$

The L_n are formally infinite integrals that needs to be absorbed by the parameters of the EFT.

The irreducible self-energy using the excited-state core field instead is obtained in the same way as above and the result is

$$i\Sigma_*(E) = -ig_*^2 \left[L_3 + (k_{\text{C}}^2 + k_*^2)L_1 + (k_{\text{C}}^2 k_*^2 + k_*^4)J^{\text{fin}}(k_*) \right], \tag{B.36}$$

where $k_* = \sqrt{2m_{\text{R}}(E - E_*)}$ is the momentum relevant for the system with an excited core field.

We can solve the finite integral J^{fin} using the integral representation of the polygamma function, where we have defined $\eta = k_{\text{C}}/k$ and $\eta' = k_{\text{C}}/p$ below,

$$\psi(i\eta) + \frac{1}{2i\eta} - \log(i\eta) = -2 \int_0^{\infty} d\eta' \frac{\eta'}{\eta'^2 - \eta^2} \frac{1}{\exp 2\pi\eta' - 1} \tag{B.37}$$

$$\begin{aligned}
&= -2 \int_{\infty}^0 dp (-k_{\text{C}}/p^2) \frac{k_{\text{C}}/p}{k_{\text{C}}^2/p^2 - k_{\text{C}}^2/k^2} \frac{1}{\exp 2\pi k_{\text{C}}/p - 1} \\
&= \frac{k^2}{\pi k_{\text{C}}} \int_0^{\infty} dp \frac{1}{p^2 - k^2} \frac{2\pi k_{\text{C}}/p}{\exp 2\pi k_{\text{C}}/p - 1} \\
&= \frac{3\pi k^2}{k_{\text{C}} m_{\text{R}}} J^{\text{fin}}(k). \tag{B.38}
\end{aligned}$$

Thus, we have

$$J^{\text{fin}}(k) = \frac{m_{\text{R}} k_{\text{C}}}{3\pi k^2} \left(\psi(i\eta) + \frac{1}{2i\eta} - \log(i\eta) \right). \tag{B.39}$$

The elastic scattering t-matrix can be written as, using the full dicluster propagator Eq. (3.43) and the P-wave integral Eq. (B.23),

$$\begin{aligned} iT_1(E) &= ig^2 D(E) (\mathbf{X}^+)^* \cdot \mathbf{X}^- \\ &= ig^2 D(E) \exp(2i\sigma_1) p^2 C(1, \eta)^2 \end{aligned} \quad (\text{B.40})$$

and in terms of the phase shift δ_1 the t-matrix is

$$T_1(E_{\mathbf{p}}) = \frac{6\pi}{m_{\text{R}}} \frac{p^2 \exp(2i\sigma_1)}{p^3 (\cot \delta_1 - i)}. \quad (\text{B.41})$$

The Coulomb-modified ERE for a P-wave interaction is given from Eq. (A.13) as

$$k^3 C(1, \eta)^2 (\cot \delta_1 - i) + 2k_{\text{C}} h_1(\eta) = -\frac{1}{a_1} + \frac{1}{2} r_1 k^2 + \dots \quad (\text{A.13})$$

However, for the case that we are studying we have both a ground- and an excited-state core field. Therefore the ERE relevant for us is given by

$$k^3 C(1, \eta)^2 (\cot \delta_1 - i) + 2k_{\text{C}} \left(h_1(\eta) + \frac{g_*^2}{g^2} h_1(\eta_*) \right) = -\frac{1}{a_1} + \frac{1}{2} r_1 k^2 + \dots, \quad (\text{B.42})$$

where the additional term comes from the fact that the dicluster propagator gets contributions also from the excited-state core field. Now, using the ERE Eq. (B.42), we can match equations (B.40) and (B.41), together with Eqs. (3.43), (B.33) and (B.36) to arrive at the low energy scattering parameters in terms of the parameters of the EFT Δ, g, g_* , from the Lagrangian (3.36):

$$a_1 = -\frac{m_{\text{R}}}{6\pi} \left[\frac{\Delta}{g^2} - \left(1 + \frac{g_*^2}{g^2} \right) L_3 - \left(k_{\text{C}}^2 + k_{\text{C}}^2 \frac{g_*^2}{g^2} - 2m_{\text{R}} E_* \frac{g_*^2}{g^2} \right) L_1 \right]^{-1} \quad (\text{B.43})$$

$$r_1 = \frac{12\pi}{m_{\text{R}}} \left[\frac{\nu}{2m_{\text{R}} g^2} - \left(1 + \frac{g_*^2}{g^2} \right) L_1 \right] \quad (\text{B.44})$$

These are the renormalization conditions for the P-wave system. Note also that we have the matching

$$2k_{\text{C}} h_1(\eta) = \frac{6\pi}{m_{\text{R}}} k^4 (1 + \eta^2) J^{\text{fn}}(k). \quad (\text{B.45})$$

To calculate bound state observables, such as form factors and capture

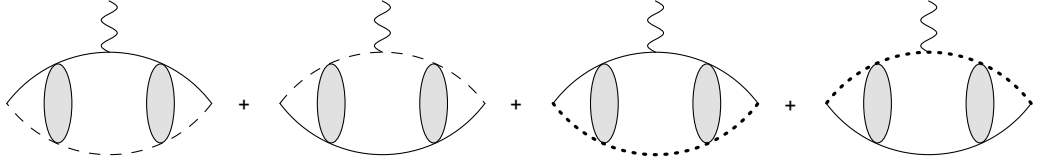


Figure B.4: The charge form factor loop-diagrams for a P-wave one-proton halo, with both a ground- state and excited-state core field included. The photon couples either to the ground- or excited-state core field or the proton field.

cross sections, we need the wavefunction renormalization. It is given by

$$\mathcal{Z} = \left[\frac{d(D^{-1})}{dE} \right]^{-1} \Big|_{E=-B} = \frac{1}{\nu + \Sigma'(-B) + \Sigma'_*(-B)} \quad (\text{B.46})$$

$$= \frac{6\pi}{g^2 m_R^2} \left[r_1 - \frac{2k_C}{m_R} \frac{d}{dE} \left(h_1(\eta) + \frac{g_*^2}{g^2} h_1(\eta_*) \right) \right]^{-1} \Big|_{E=-B}, \quad (\text{B.47})$$

using Eqs. (3.43), (B.33), (B.36) and (B.45). Note that the wavefunction renormalization consists of two undetermined parameters r_1 and g_*/g , that is we need to fix in total three parameters at LO to be able to make predictions using both the ground- and excited-state core fields.

B.4 P-wave charge form factor

For a P-wave interaction there are two charge form factor diagrams that are needed at LO. These diagrams are shown in Figs. 3.4(a) and B.4. In this appendix we write down these diagrams and show how they give the charge form factor of the system.

B.4.1 Charge form factor diagrams

The loop-diagram in Fig. B.4 consists of a proton-core bubble, where the external photon line couples to either the ground-state core, excited-state core or the proton. The shaded blobs denote the Coulomb resummation and they are simply given by Coulomb propagators. Let us start by writing down the loop-diagram using only the ground-state core field. In momentum-space

this loop-diagram is given by

$$\begin{aligned}
i\Gamma_{\text{loop,g.s.}}(\mathbf{Q}) &= -i \frac{g^2 e Z_c}{3} \int \frac{d^3 k_1 d^3 k_2 d^3 k_3}{(2\pi)^9} \mathbf{k}_3 \cdot \mathbf{k}_1 \langle \mathbf{k}_3 | G_C(-B) | \mathbf{k}_2 - f\mathbf{Q}/2 \rangle \\
&\quad \times \langle \mathbf{k}_2 + f\mathbf{Q}/2 | G_C(-B) | \mathbf{k}_1 \rangle \\
&\quad + \left[(f \rightarrow 1-f), (Z_c \rightarrow 1) \right]. \tag{B.48}
\end{aligned}$$

Note that in writing down Eq. (B.48) we have replaced the P-wave proton-core interaction vertices with $g^2 \mathbf{k}_2 \cdot \mathbf{k}_1/3$, in the same way as was done in Appendix B.3.1. Doing Fourier transforms on the middle momentum-space ket and bra and then using equation (B.29) we simplify Eq. (B.48) to

$$\begin{aligned}
i\Gamma_{\text{loop,g.s.}}(\mathbf{Q}) &= -i \frac{g^2 e Z_c}{3} \int \frac{d^3 k_1 d^3 k_2 d^3 k_3}{(2\pi)^9} d^3 r_1 d^3 r_2 \mathbf{k}_3 \cdot \mathbf{k}_1 \langle \mathbf{k}_3 | G_C(-B) | \mathbf{r}_1 \rangle \\
&\quad \times \exp(i\mathbf{k}_2 \cdot (\mathbf{r}_2 - \mathbf{r}_1)) \exp(if\mathbf{Q} \cdot (\mathbf{r}_1 + \mathbf{r}_2)/2) \langle \mathbf{r}_2 | G_C(-B) | \mathbf{k}_1 \rangle \\
&\quad + \left[(f \rightarrow 1-f), (Z_c \rightarrow 1) \right] \\
&= -i3g^2 e Z_c \int d^3 r \exp(if\mathbf{Q} \cdot \mathbf{r}) \left| \lim_{r' \rightarrow 0} \left(\frac{G_C^{(1)}(-B; r', r)}{r'} \right) \right|^2 \\
&\quad + \left[(f \rightarrow 1-f), (Z_c \rightarrow 1) \right]. \tag{B.49}
\end{aligned}$$

The limit of the Coulomb Green's function we replace using Eq. (A.28)

$$\lim_{r' \rightarrow 0} \left(\frac{G_C^{(1)}(-B; r', r)}{r'} \right) = -\frac{m_R \gamma}{6\pi} \Gamma(2 + k_C/\gamma) \frac{W_{-k_C/\gamma, 3/2}(2\gamma r)}{r}. \tag{A.28}$$

Note that the order Q^0 integral in Eq. (B.49) is divergent. This is why the tree-level diagram in Fig. 3.4(a) is needed at LO, such that the observable charge form factor is finite. The order Q^2 integral is finite and it is straightforward to evaluate this piece, using the partial-wave projected Coulomb Green's function (A.28).

The loop-diagram with the excited-state core field is derived in the same fashion as above and the result is

$$\begin{aligned}
i\Gamma_{\text{loop,e.s.}}(\mathbf{Q}) &= -i3g_*^2 e Z_c \int d^3 r \exp(if\mathbf{Q} \cdot \mathbf{r}) \left| \lim_{r' \rightarrow 0} \left(\frac{G_C^{(1)}(-B - E_*; r', r)}{r'} \right) \right|^2 \\
&\quad + \left[(f \rightarrow 1-f), (Z_c \rightarrow 1) \right], \tag{B.50}
\end{aligned}$$

with E_* being the excited state energy and with

$$\lim_{r' \rightarrow 0} \left(\frac{G_C^{(1)}(-B - E_*; r', r)}{r'} \right) = -\frac{m_R \gamma_*}{6\pi} \Gamma(2 + k_C/\gamma_*) \frac{W_{-k_C/\gamma_*, 3/2}(2\gamma_* r)}{r} \quad (\text{B.51})$$

from Eq. (A.28).

The tree-level diagram in Fig. 3.4(a) is given by

$$i\Gamma_{\text{tree}} = i\nu e(Z_C + 1) , \quad (\text{B.52})$$

from the photon-dicluster interaction vertex.

The charge form factor is given in terms of the diagrams as

$$F_C(Q) = \frac{\mathcal{Z}}{e(Z_C + 1)} [\Gamma_{\text{loop, g.s.}}(Q) + \Gamma_{\text{loop, g.s.}}(Q) + \Gamma_{\text{tree}} + \dots] , \quad (\text{B.53})$$

where the dots refer to higher-order diagrams that we do not consider here.

B.4.2 Normalization of the charge radius

The normalization of the charge form factor for a P-wave interaction proceeds in the same way as in Chapter 3.1.3 for S-waves.

First we note that the loop-diagram (B.48) reduces to a derivative of the irreducible self-energy at $Q = 0$, using the spectral representation of the Coulomb Green's function (A.1) and the definition of the vector quantity \mathbf{X}_1 (B.16):

$$\begin{aligned} \Gamma_{\text{loop, g.s.}}(0) &= -\frac{g^2 e(Z_C + 1)}{3} \int \frac{d^3 p}{(2\pi)^3} \frac{\mathbf{X}_1(E_{\mathbf{p}}) \cdot \mathbf{X}_2^*(E_{\mathbf{p}})}{[E - \mathbf{p}^2/(2m_R)]^2} \\ &= e(Z_C + 1)\Sigma'(-B) \end{aligned} \quad (\text{B.54})$$

In the same way we have the $Q = 0$ limit of the excited-state loop-diagram

$$\Gamma_{\text{loop, e.s.}}(0) = e(Z_C + 1)\Sigma'_*(-B) . \quad (\text{B.55})$$

Now, using the charge form factor formula (B.53) and the wavefunction renormalization (B.46) we arrive at the correct normalization

$$F_C(0) = 1 . \quad (\text{B.56})$$

B.4.3 The charge radius

Now that we have shown that the charge form factor is properly normalized we will use this in Eq. (B.53) to get a simple expression for the charge radius of the system. Eq. (B.53) now amounts to

$$\begin{aligned} F_C(Q) &= \frac{\mathcal{Z}}{e(Z_c + 1)} \left(\Gamma_{\text{tree}} + \Gamma_{\text{loop}}(0) + \frac{1}{2} \Gamma_{\text{loop}}'' Q^2 \right) + \dots \\ &= 1 + \frac{\mathcal{Z}}{e(Z_c + 1)} \Gamma_{\text{loop}}^{(2)} Q^2 + \dots, \end{aligned} \quad (\text{B.57})$$

where we have defined $\Gamma_{\text{loop}}(Q) = \Gamma_{\text{loop, g.s.}}(Q) + \Gamma_{\text{loop, e.s.}}(Q)$. Thus the charge radius is given by

$$r_C^2 = -3 \frac{\mathcal{Z}}{e(Z_c + 1)} \Gamma_{\text{loop}}'', \quad (\text{B.58})$$

that is we simply need to evaluate the integrals (B.49) and (B.50) and we do this by numerical integration.

Bibliography

- [1] I. Tanihata, H. Hamagaki, O. Hashimoto, Y. Shida, N. Yoshikawa, et al., Measurements of Interaction Cross-Sections and Nuclear Radii in the Light p Shell Region, *Phys. Rev. Lett.* 55 (1985) 2676–2679.
- [2] P. Hansen, B. Jonson, The Neutron halo of extremely neutron-rich nuclei, *Europhys. Lett.* 4 (1987) 409–414.
- [3] P. Hansen, A. Jensen, B. Jonson, Nuclear halos, *Ann. Rev. Nucl. Part. Sci.* 45 (1995) 591–634.
- [4] C. Bertulani, H.-W. Hammer, U. van Kolck, Effective field theory for halo nuclei, *Nucl. Phys. A* 712 (2002) 37–58.
- [5] P. F. Bedaque, H.-W. Hammer, U. van Kolck, Narrow resonances in effective field theory, *Phys. Lett.* B569 (2003) 159–167.
- [6] J. Rotureau, U. van Kolck, Effective Field Theory and the Gamow Shell Model: The ${}^6\text{He}$ Halo Nucleus, *Few Body Syst.* 54 (2013) 725–735.
- [7] C. Ji, C. Elster, D. Phillips, The ${}^6\text{He}$ Nucleus in Halo EFT (2014). [arXiv:1405.2394](https://arxiv.org/abs/1405.2394).
- [8] G. Hagen, P. Hagen, H.-W. Hammer, L. Platter, Efimov Physics Around the Neutron-Rich ${}^{60}\text{Ca}$ Isotope, *Phys. Rev. Lett.* 111 (13) (2013) 132501. [arXiv:1306.3661](https://arxiv.org/abs/1306.3661).
- [9] B. Acharya, C. Ji, D. Phillips, Implications of a matter-radius measurement for the structure of Carbon-22, *Phys. Lett.* B723 (2013) 196–200. [arXiv:1303.6720](https://arxiv.org/abs/1303.6720).
- [10] H.-W. Hammer, D. R. Phillips, Electric properties of the Beryllium-11 system in Halo EFT, *Nucl. Phys. A* 865 (2011) 17–42.

- [11] G. Rupak, L. Fernando, A. Vaghani, Radiative Neutron Capture on Carbon-14 in Effective Field Theory, *Phys. Rev. C* **86** (2012) 044608. arXiv:1204.4408.
- [12] B. Acharya, D. R. Phillips, Carbon-19 in Halo EFT: Effective-range parameters from Coulomb-dissociation experiments, *Nucl. Phys. A* **913** (2013) 103–115.
- [13] X. Zhang, K. M. Nollett, D. Phillips, Marrying *ab initio* calculations and Halo-EFT: the case of ${}^7\text{Li} + n \rightarrow {}^8\text{Li} + \gamma$, *Phys. Rev. C* **89** (2014) 024613. arXiv:1311.6822.
- [14] R. Higa, H.-W. Hammer, U. van Kolck, $\alpha\alpha$ scattering in halo effective field theory, *Nucl. Phys. A* **809** (2008) 171.
- [15] L. S. Brown, G. M. Hale, Field Theory of the $d+t \rightarrow n+\alpha$ Reaction Dominated by a ${}^5\text{He}^*$ Unstable Particle, *Phys. Rev. C* **89** (2014) 014622. arXiv:1308.0347.
- [16] D. B. Kaplan, M. J. Savage, M. B. Wise, A Perturbative calculation of the electromagnetic form-factors of the deuteron, *Phys. Rev. C* **59** (1999) 617–629. arXiv:nucl-th/9804032.
- [17] X. Kong, F. Ravndal, Coulomb effects in low-energy proton proton scattering, *Nucl. Phys. A* **665** (2000) 137–163. arXiv:hep-ph/9903523.
- [18] E. Adelberger, A. Balantekin, D. Bemmerer, C. Bertulani, J.-W. Chen, et al., Solar fusion cross sections II: the pp chain and CNO cycles, *Rev. Mod. Phys.* **83** (2011) 195. arXiv:1004.2318.
- [19] G. Wallerstein, I. Iben, P. Parker, A. M. Boesgaard, G. M. Hale, A. E. Champagne, C. A. Barnes, F. Käppeler, V. V. Smith, R. D. Hoffman, F. X. Timmes, C. Sneden, R. N. Boyd, B. S. Meyer, D. L. Lambert, Synthesis of the elements in stars: forty years of progress, *Rev. Mod. Phys.* **69** (1997) 995–1084.
- [20] M. E. Peskin, D. V. Schroeder, An introduction to quantum field theory, Advanced book program, Westview Press Reading (Mass.), Boulder (Colo.), 1995.
- [21] D. B. Kaplan, M. J. Savage, M. B. Wise, A New expansion for nucleon-nucleon interactions, *Phys. Lett. B* **424** (1998) 390–396. arXiv:nucl-th/9801034.

- [22] X. Zhang, K. M. Nollett, D. Phillips, Marrying ab initio calculations and Halo EFT: the case of ${}^7\text{Be} + p \rightarrow {}^8\text{B} + \gamma$, Phys. Rev. C89 (2014) 051602. arXiv:1401.4482.
- [23] X. Kong, F. Ravndal, Proton proton scattering lengths from effective field theory, Phys. Lett. B450 (1999) 320–324. arXiv:nucl-th/9811076.
- [24] X. Kong, F. Ravndal, Proton proton fusion in leading order of effective field theory, Nucl. Phys. A656 (1999) 421–429. arXiv:nucl-th/9902064.
- [25] S.-i. Ando, M. C. Birse, Effective field theory of ${}^3\text{He}$, J. Phys. G37 (2010) 105108. arXiv:1003.4383.
- [26] J. Vanasse, D. A. Egolf, J. Kerin, S. König, R. P. Springer, ${}^3\text{He}$ and pd Scattering to Next-to-Leading Order in Pionless Effective Field Theory (2014). arXiv:1402.5441.
- [27] J. Huang, C. Bertulani, V. Guimaraes, Radiative capture of nucleons at astrophysical energies with single-particle states (2008). arXiv:0810.3867.
- [28] C. Gagliardi, R. Tribble, A. Azhari, H. Clark, Y. Lui, et al., Tests of transfer reaction determinations of astrophysical S - factors, Phys. Rev. C59 (1999) 1149–1153. arXiv:nucl-ex/9811005.
- [29] D. Tilley, H. Weller, C. Cheves, Energy levels of light nuclei $A = 16-17$, Nucl. Phys. A 564 (1993) 1–183.
- [30] A. Blue, W. Haeberli, Polarization of Protons Elastically Scattered by Oxygen, Phys. Rev. 137 (1965) B284.
- [31] S. König, D. Lee, H.-W. Hammer, Causality constraints for charged particles, J. Phys. G: Nucl. Part. Phys. 40 (2013) 045106.
- [32] K. Bennaceur, F. Nowacki, J. Okołowicz, M. Płoszajczak, Analysis of the capture reaction using the shell model embedded in the continuum, Nucl. Phys. A 671 (2000) 203–232.
- [33] R. Morlock, R. Kunz, A. Mayer, M. Jaeger, A. Müller, J. Hammer, P. Mohr, H. Oberhummer, G. Staudt, V. Kölle, Halo Properties of the First $1/2+$ State in $F17$ from the $O16(p,\gamma)F17$ Reaction, Phys. Rev. Lett. 79 (1997) 3837–3840.

- [34] H. C. Chow, G. M. Griffiths, T. H. Hall, The $^{16}\text{O}(p,\gamma)^{17}\text{F}$ direct capture cross section with an extrapolation to astrophysical energies, *Can. J. Phys.* 53 (1975) 1672–1686.
- [35] K. M. Nollett, R. Wiringa, Asymptotic normalization coefficients from ab initio calculations, *Phys. Rev. C* 83 (2011) 041001. arXiv:1102.1787.
- [36] P. Navrátil, R. Roth, S. Quaglioni, Ab initio many-body calculation of the $^7\text{Be}(p,\gamma)^8\text{B}$ radiative capture, *Phys. Lett. B* 704 (2011) 379–383. arXiv:1105.5977.
- [37] G. Tabacaru, A. Azhari, J. Brinkley, V. Burjan, F. Carstoiu, et al., Scattering of Be-7 and B-8 and the astrophysical $S(17)$ factor, *Phys. Rev. C* 73 (2006) 025808. arXiv:nucl-ex/0508029.
- [38] B. Filippone, A. Elwyn, C. Davids, D. Koetke, Measurement of the Be-7 (p, gamma) B-8 Reaction Cross Section at Low Energies, *Phys. Rev. Lett.* 50 (1983) 412–416.
- [39] F. Hammache, G. Bogaert, P. Aguer, C. Angulo, S. Barhoumi, et al., New measurement and analysis of the Be-7 (p, gamma) B-8 cross-section, *Phys. Rev. Lett.* 80 (1998) 928–931. arXiv:nucl-ex/9712003.
- [40] F. Hammache, G. Bogaert, P. Aguer, C. Angulo, S. Barhoumi, et al., Low-energy measurement of the Be-7(p,gamma) B-8 cross-section, *Phys. Rev. Lett.* 86 (2001) 3985–3988. arXiv:nucl-ex/0101014.
- [41] M. Hass, et al., A new measurement of the Be-7(p,gamma)B-8 cross-section with an implanted Be-7 target, *Phys. Lett. B* 462 (1999) 237–242.
- [42] F. Strieder, et al., Absolute cross section of $^7\text{Be}(p,\gamma)^8\text{B}$, *Nucl. Phys. A* 696 (2001) 219–230.
- [43] L. Baby, et al., A New precision measurement of the Be-7(p,gamma) B-8 cross-section with an implanted Be-7 target, *Phys. Rev. Lett.* 90 (2003) 022501. arXiv:nucl-ex/0208005.
- [44] A. Junghans, E. Mohrmann, K. Snover, T. Steiger, E. Adelberger, et al., Precise measurement of the Be-7(p,gamma) B-8 S factor, *Phys. Rev. C* 68 (2003) 065803. arXiv:nucl-ex/0308003.
- [45] A. Junghans, K. Snover, E. Mohrmann, E. Adelberger, L. Buchmann, Updated S factors for the Be-7 (p, gamma) B-8 reaction, *Phys. Rev. C* 81 (2010) 012801.